Chemical Reactor Modeling of Oxides of Nitrogen in Lean-Premixed, High-Intensity Combustion of Carbon Monoxide-Hydrogen Blends

Gwenn Heyer

A thesis
submitted in partial fulfillment of the
requirements for the degree of

Master of Science in Mechanical Engineering

University of Washington

2004

Program Authorized to Offer Degree:
Mechanical Engineering

University of Washington
Graduate School

This is to certify that I have examined this copy of a master's thesis by

Gwenn Heyer

and have found that it is complete and satisfactory in all respects,
and that any and all revisions required by the final
examining committee have been made.

Committee Members:

_____
Philip C. Malte

_____
John C. Kramlich

_____
Teodora R. Shuman

Date:_____

In presenting this thesis in partial fulfillment of the requirements for a master's degree at the University of Washington, I agree that the Library shall make its copies freely available for inspection. I further agree that extensive copying of this thesis is allowable only for scholarly purposes, consistent with "fair use" as prescribed in the U.S. Copyright Law. Any other reproduction for any purposes or by any means shall not be allowed without my written permission.

Signature _____

Date _____

TABLE OF CONTENTS

Page

LIST OF FIGURES

Figure Number Page

LIST OF TABLES

Table Number Page

ACKNOWLEDGEMENTS

The author wishes to express sincere appreciation to Professor Philip C. Malte for his insight throughout the completion of this research. Dr. Malte has very generously offered his time and expertise in order to provide me with both academic and professional guidance.

Thank you to Professors John Kramlich and Teodora Shuman for their assistance throughout the completion of this thesis.

DEDICATION

To my Mom,
who taught me the values of hard work, determination, and helping others.
Her encouragement and support have helped me reach my goals.

Section 1: Introduction

Background on Energy Use and CO/H_2 Fuels

Between 2000 and 2020, U.S. energy consumption is projected by the Energy Information Administration to increase by about 32%. Because of this, U.S. natural gas demand is projected to increase by more than 50%, from 22.8 to 34.7 trillion cubic feet per year. Growth is projected in all sectors – industrial, commercial, residential, transportation, and power generation. More than half of the overall increase in natural gas consumption will result from the rising demand for power generation.[1]

One aspect of the present energy crisis is an increased dependence, not only on foreign oil, but on a narrow range of energy options. As Figure 1 shows, natural gas is currently only the third largest source of U.S. power generation at 16%. But, more importantly, about 90% of all new electricity plants currently under construction will be fueled by natural gas. While natural gas has many advantages, an over-reliance on natural gas may leave consumers vulnerable to price spikes and supply disruptions. Matching the sharply increasing projected demand for natural gas with adequate supplies is a significant long-term challenge. As of 2002, the domestic proven natural gas reserves were only 186.9 trillion cubic feet.[2] Therefore, meeting demand will likely require substantial dependence on imported natural gas and new natural gas exploration on environmentally-fragile areas. Meeting our energy needs through strategic use of our fuel resources is crucial.

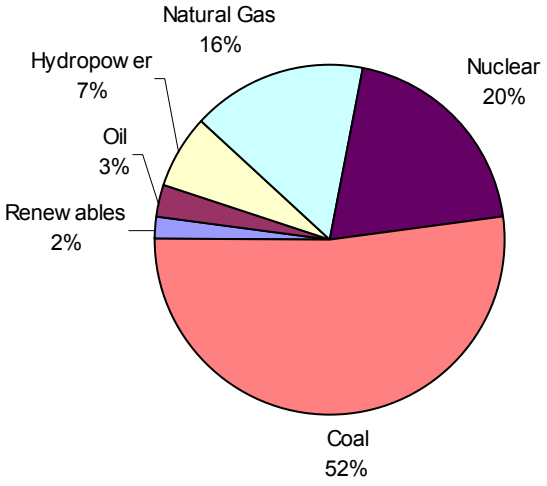

Figure 1, Fuel Sources for Electricity Generation in 2000[1]

The U.S. has enough coal to last for 250 years, far surpassing reserves of natural gas. After peaking in 1982, coal prices have generally declined. This trend is projected to continue through 2020, reflecting an expanding shift into lower-cost western coal production and substantial increases in productivity. Furthermore, the supply of coal is elastic in that increased demand can easily be met by increasing mining rates. Using coal as our dominant energy source is an important step toward energy independence, and in the long term, toward ensuring inexpensive energy prices. Special attention, however, must be given to the Clean Air Act Amendments of 1990 and related state regulations requiring electricity generators to reduce emissions of sulfur dioxide (SO_2) and nitric oxide (NO), common pollutants of coal combustion.

Research into cleaner coal technologies, such as the integrated gasification combined cycle (IGCC), may increase the attractiveness of coal as a fuel for new generation power plants. In IGCC, coal is generally gasified with oxygen instead of air to decrease the volume of the fuel gas, making cleanup easier. Gasifying coal with sub-stoichiometric oxygen gives a fuel/synthesis gas composed of CO, H_2, CO_2, and H_2O. The synthesis gas is cleaned of sulfur and particulate matter, then burned in a combined cycle system. The

process emits significantly less SO_2, NO_x, particulate matter, and mercury than the traditional pulverized coal steam power plants. The use of coal IGCC is cost competitive with capital costs of about \$1100/kw_e and electricity costs of 4-5 cents per kwh.[3] The wholesale electricity costs of 4-5 cents per kwh is similar to that of combined cycle gas turbine systems burning \$6/MMBTU natural gas. IGCC also allows for the synthesis gas of H_2, CO, H_2O, and CO_2 to be used with water-gas shift, opening up the possibility of an H_2-H_2O fuel, with the CO_2 separated and sequestered.

Some gas turbine manufacturers are now developing lean-premixed combustors for CO/H_2 fuels. Thus, there is a pressing need to develop robust engineering models for predicting NO_x formation from CO/H_2 mixtures burned in lean-premixed combustors. While much attention has been devoted to modeling the NO_x formation from natural gas fuel combustors, uncertainties exist in modeling NO_x from CO/H_2 combustion. Thus, research needs to be done to fill in this gap.

Formation Pathways of NO_x

Most of the nitric oxide (NO) formed in combustion will oxidize to NO_2, either in the downstream sections of the heat engine, in the exhaust stack, or in the atmosphere. As a result, it is customary to express results as oxides of nitrogen (NO_x), the sum of NO and NO_2. In CO/H_2 combustion, NO can be produced by three reaction pathways:

1. Zeldovich Pathway

$$N_2 + O = NO + N$$
$$N + O_2 = NO + O$$
$$N + OH = NO + H$$

The Zeldovich pathway produces NO by the oxidation of atmospheric nitrogen in high temperature regions of the flame and in the post flame gases. The process proceeds at a significant rate only at temperatures above around 1850K and formation is controlled largely by flame temperature.[4] For this reason, NO produced from this pathway is often termed *thermal NO.*

2. Nitrous Oxide (N_2O) Pathway

$$N_2 + O + M = N_2O + M$$
$$N_2O + O = NO + NO$$
$$N_2O + H = NO + NH$$

The nitrous oxide pathway is driven by super-equilibrium levels of O-atom and H-atom in the flame zone and immediate post-flame zone.

3. NNH Pathway

$$N_2 + H = NNH$$
$$N_2 + H + M = NNH + M$$
$$NNH + O = N_2O + H$$
$$NNH + O_2 = N_2O + OH$$
$$NNH + O = NO + NH$$

NNH is formed quickly during combustion, and then destroyed quickly. Thus, its effect is mainly restricted to the flame zone and is strongly influenced by the super-equilibrium levels of O-atom and H-atom.

Purpose of Study

The GRI 3.0 mechanism has been widely and successfully used to predict NO_x from methane and air combustion.[5] Limited reactor modeling for CO/H_2 combustion has been done. Preliminary results from the GRI 3.0 mechanism using a reactor element configuration that has worked well for hydrocarbon fuels significantly over predict NO_x for CO/H_2 fuels. The Combustion Laboratory at the University of Washington has databases of both hydrocarbon and CO/H_2 fuel combustion emissions for bench-scale, high-intensity burners. Initially the trends in NO_x production with fuel C/H ratio were examined for both the hydrocarbon and CO/H_2 databases. The emphasis of this modeling, however, is placed on CO/H_2 fuels. The hydrocarbon results may be found in Appendix A.

The goal of this study is to develop a robust chemical reactor model for predicting formation of NO_x from CO/H_2 combustion at both 1 atm and elevated pressure (6.5 atm in the existing database) in lean-premixed, high-intensity flames with temperatures near 1800 K. In this thesis, first, overall trends in NO_x are discussed from compilation of the data taken by Malte,[6] Jarrett,[7] and Horning.[8] Next, a combustion reactor element configuration is found that attempts to match both NO_x and CO emissions from the experiments. This configuration is used to test the NO_x predictions and formation pathways of several mechanisms. This modeling leads to a useful mechanism and element configuration for predicting NO_x and CO for CO/H_2 combustion at atmospheric and elevated pressure.

Section 2: Experimental Databases

Explanation of Experiments

The 64 cm^3 atmospheric jet-stirred reactor (JSR) of Malte's experiments[6] uses an inlet nozzle of diameter 5.6 mm. As shown by Figure 2, the temperature and gas sampling is done in the recirculation zone of the reactor. A 30° C correction was applied to measured temperatures to account for thermocouple radiation losses. Malte's experiments used CO/H_2 molar ratios of 0.33, 1, and 3, preheat temperatures between 150-250° C, residence times near 3.6 ms, fuel-air equivalence ratios (Φ) near 0.6, and flame temperatures near 1790 K.[6]

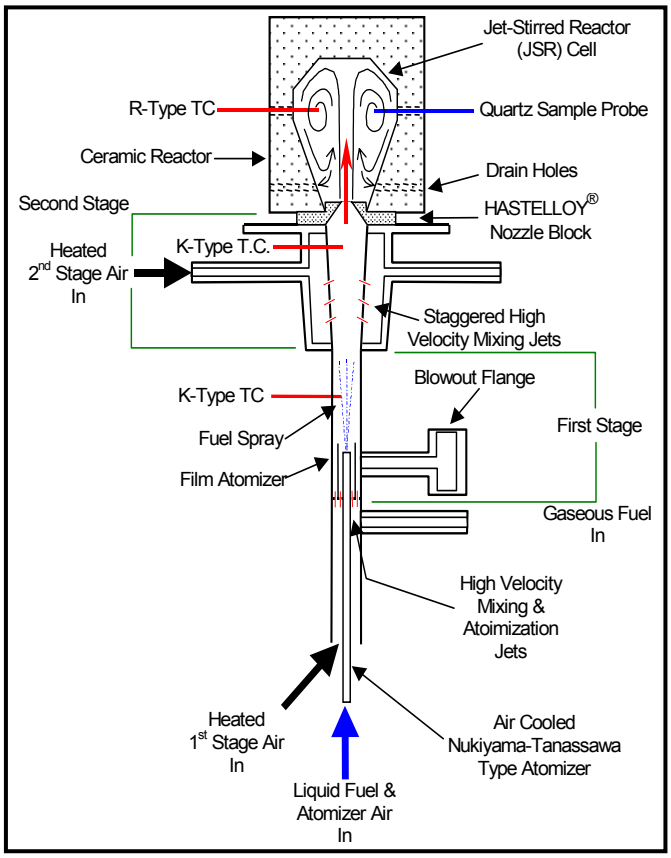

Figure 2, Schematic of the Atmospheric JSR with Premixing Injector

Figure 3 shows the JSR during testing. The gas sampling is done on the left-hand side while the temperature is taken on the right.

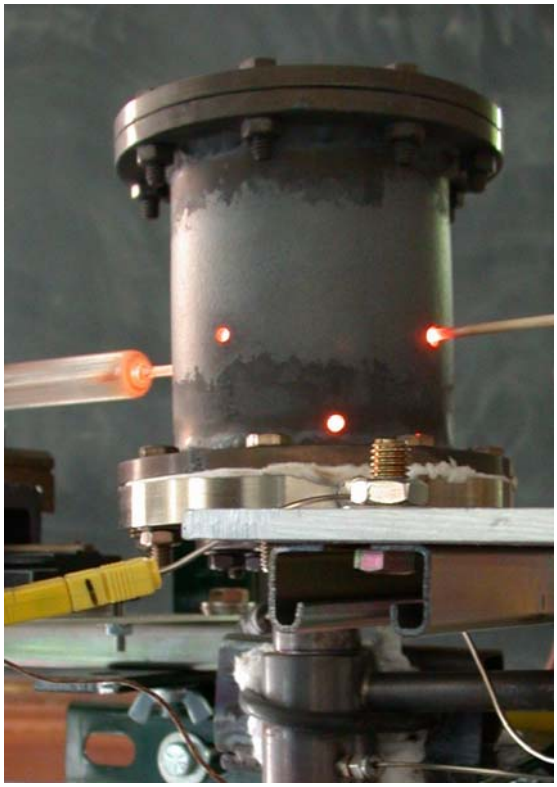

Figure 3, Atmospheric JSR During Testing

The atmospheric JSR used by Jarrett was 15.8 cm^3. Jarrett tested CO/H_2 ratios of 0.5, 1, and 2 with no preheat, residence times of 3.7-4.6 ms, equivalence ratios of 0.41-0.64, and flame temperatures of 1400-1800 K.[7] The experiments by Horning were done using a 2 cm^3 high-pressure JSR and an inlet nozzle of 1 mm diameter. Horning took measurements at CO/H_2 ratios of 0.5 and 1, using no preheat, residence times near 4 ms, equivalence ratios near 0.5, and flame temperatures from 1680-1890 K. In addition, at a constant temperature of 1785 K, Horning measured NO_x for seven CO/H_2 ratios between 0.5 and 3.2.[8]

Examination of Databases

The compilation of NO_x data from Malte,[6] Jarrett,[7] and Horning[8] is shown in Figure 4. The first set of Horning's data has been interpolated to 1795 K from the 1680-1890 K temperature range. The NO_x measurements from Malte and Horning for any given CO/H_2 ratio agree well. The lower NO_x measurements of Horning's experiments, despite the slightly greater residence times, can be attributed to the greater pressure.[4]

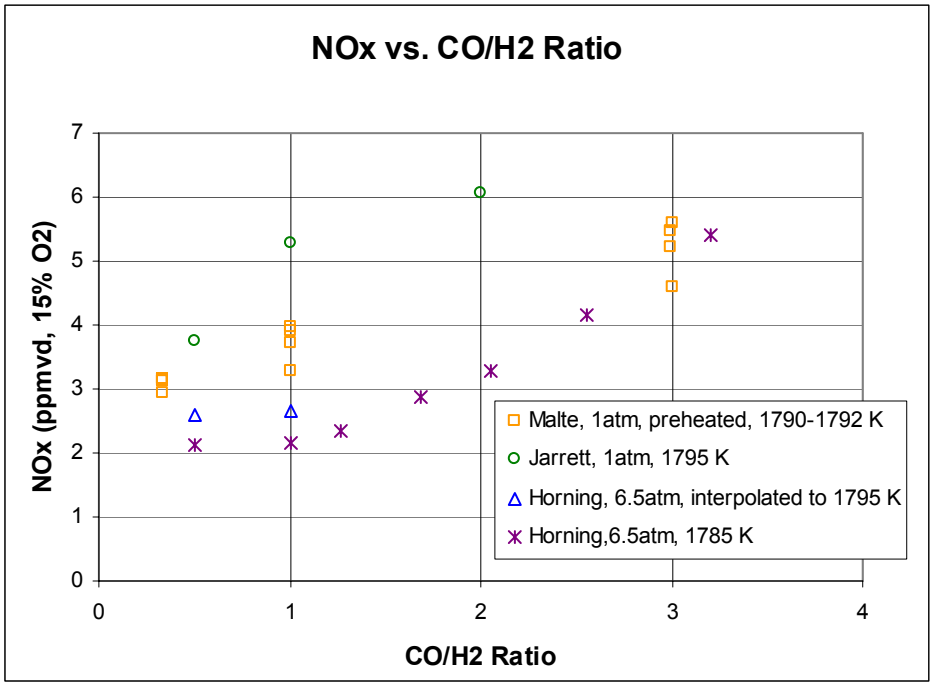

Figure 4, Compilation of NO_x Data from Malte, Jarrett, and Horning

Jarrett's data does not compare well with the data of Malte and Horning. This is also the case for the hydrocarbon data, as shown in Appendix A. Jarrett's data, therefore, is excluded from this study.

Section 3: Determination of Reactor Element Configuration

Flame Speed Influence on Reactor Element Configuration

The air and fuel mixture entering the JSR is first engulfed in the flame. The flame is anchored over and around the inlet jet, taking up only a small percentage of the reactor volume. Given sufficiently-long residence times (of about 4 ms), as in the experiments of Malte and Horning, a post-flame environment will follow. The post-flame region takes up the remaining, larger part of the reactor volume, and is characterized by the burning flow impinging on the top wall of the reactor and recirculating downward.

In recent studies, the flame and post-flame volumes have been modeled using two perfectly-stirred reactor (PSR) elements in series.[8,9,10] To represent the non-equilibrium turbulent flame, the first PSR is specified as a PSB – adiabatic and of length determined to be the shortest possible without blowout. The second PSR represents the post-flame region. It is specified as a PST, and therefore assigned the temperature measured for the recirculation zone.

In order to critique this two-PSR configuration, the fraction of the reactor volume associated with the first PSR may be based on the turbulent flame thickness, δ_T, and used to evaluate the size of the non-equilibrium flame zone.[9] The turbulent flame thickness is determined by analogy to the laminar flame thickness as the ratio of the turbulent diffusivity ($D_T \approx u' l_o$) to the turbulent burning velocity, S_T. Therefore, $\delta_T \approx u' d_o / S_T$. The turbulent intensity, u', is assumed to be 10% of the inlet jet (cold) velocity.[9] The turbulence integral scale, l_o is assumed to be the inlet jet diameter, d_o. The turbulent velocity, S_T is based on the equation: $S_T = S_L + u'(1+Da^{-2})^{-1/4}$ where S_L is the laminar burning velocity and the Damköhler number, Da, is the ratio of the mixing time (τ_m) to the chemical time (τ_l).[11] The mixing time is calculated as d_o/u'. The chemical time is calculated as α/S_L^2, where α is the thermal diffusivity and dependent on inlet temperature

and reactor pressure. Finally, the flame volume is a function of the turbulent flame thickness and is about equal to $5\pi\delta_T^3$, as developed by Rutar et al.[9]

The first step in determining the turbulent flame thickness for each set of experimental conditions is to determine the laminar flame speed of the fuel mixture at a given Φ and CO/H_2 ratio. McLean et al.[12] show experimental data and model results for laminar flame speeds of CO/H_2=1 and CO/H_2=19 mixtures at 1 atm, 298 K, and for Φ as low as 0.6. Table 1 shows the data at CO/H_2 = 1 and 19 and Φ = 0.6, 0.7, and 0.8.

Table 1, Experimental Laminar Flame Speed of McLean at 1 atm and 298K[12]

Phi	CO%/H2%	CO/H2	SL (cm/s)
0.6	50/50	1	30.0
0.6	95/5	19	12.2
0.7	50/50	1	50.0
0.7	95/5	19	18.0
0.8	50/50	1	70.0
0.8	95/5	19	23.0

By accounting for laminar flame speed variance with CO/H_2 ratio and Φ, the data of McLean et al. are used to estimate laminar flame speeds at the experimental conditions of Horning and Malte. The CO/H_2 fuel ratios used in the experiments of Horning and Malte are near the CO/H_2=1 fuel ratio used by McLean et al. Thus, linear interpolation and extrapolation of the CO/H_2=1 and CO/H_2=19 data in Table 1 is used to determine laminar flame speeds at Φ = 0.6, 0.7, and 0.8 for the fuel molar ratios used by Horning and Malte. Next, the resulting laminar flame speeds are adjusted for equivalence ratio. The data of McLean et al. show that at low Φ, the change in laminar flame speed with Φ is nearly linear. Thus, for this study, the laminar flame speed values are extrapolated to Φ as low as 0.52 to match the experimental conditions of Horning. Table 2 shows the interpolated/extrapolated laminar flame speeds at 1 atm and 298 K with CO/H_2 ratio and Φ matching the experimental values of Horning and Malte.

Table 2, Interpolated/Extrapolated Laminar Flame Speeds at 1 atm and 298 K

	CO/H2	Phi	SL (cm/s)
Horning	0.5	0.550	20.3
	1	0.540	17.9
	1.27	0.536	17.0
	1.69	0.532	16.1
	2.05	0.529	15.4
	2.56	0.526	14.7
	3.2	0.524	14.0
Malte	0.33	0.661	38.9
	1	0.625	32.4
	3	0.628	32.9

Previous experiments using a flame holder have shown that the velocity at blow off is proportional to the laminar flame speed and both are inversely proportional to the ignition time.[13] Applying this relationship to the two-PSR model, the residence time of the blowout PSR is assumed to be inversely proportional to laminar flame speed. Therefore, multiplying the laminar flame speed at 1atm and 298 K by the ratio of PSB residence time at 1 atm and 298 K to the residence time at a new temperature and pressure condition, gives the estimated laminar flame speed at the new condition. In Horning's experiments, deviation from the laminar flame speeds at 1 atm and 298 K is only due to increased pressure. The ratio of PSB residence time at 1 atm to that at 6.5 atm was found at 298 K for CO/H_2 = 0.5, 1.69, and 3.2 and Φ = 0.6, 0.7, and 0.8. The results were then interpolated for each CO/H_2 ratio and extrapolated to the corresponding Φ. Table 3 shows the PSB(1 atm)/PSB(6.5 atm) residence time ratios and the corrected laminar flame speeds for Horning's experiments.

Table 3, Laminar Flame Speeds at Horning's Experimental Conditions

		SL	$\tau_{bo,1atm}/\tau_{bo,6.5atm}$	SL
		1 atm, 298 K	298K	6.5 atm, 298 K
CO/H2	Phi	cm/s	ms	cm/s
0.5	0.5502	20.3	2.31	47.0
1	0.5396	17.9	2.17	39.0
1.27	0.5358	17.0	2.16	36.8
1.69	0.5318	16.1	2.18	35.1
2.05	0.5291	15.4	2.21	34.0
2.56	0.5264	14.7	2.27	33.4
3.2	0.5241	14.0	2.35	32.9

In Malte's experiments, deviation from the laminar flame speeds at 1 atm and 298 K is only due to preheat temperature. The ratio of PSB residence time at 298 K to that at 423 K was found at 1 atm for CO/H_2 = 0.33, 1, and 3 and Φ = 0.6, 0.7, and 0.8. Then, the results were interpolated to the experimental Φ. Table 4 shows the PSB(298 K)/PSB (423 K) residence time ratios and the corrected laminar flame speeds for Malte's experiments.

Table 4, Laminar Flame Speeds at Malte's Experimental Conditions

		SL	$\tau_{bo,298K}/\tau_{bo,423K}$	SL
		1 atm, 298 K	1 atm	1 atm, 423 K
CO/H2	Phi	cm/s	ms	cm/s
0.33	0.661	38.9	1.42	55.3
1	0.625	32.4	1.48	47.9
3	0.628	32.9	1.46	48.0

Thermal diffusivities for air are used in the flame speed calculations. For Malte's experiments, interpolation to 423 K gives $\alpha=4.24*10^{-5}$ m^2/s.[14] Thermal diffusivity is inversely proportional to pressure. Thus, for Horning's experiments the thermal diffusivity of air, interpolated to 298K, is multiplied by 1 atm/6.5 atm to obtain $\alpha=3.42*10^{-6}$.[14] These values, combined with the laminar flame speeds in Table 4, give the chemical times. The mixing time is determined using the inlet jet diameter and turbulent intensity calculated by using the molecular weight of the mixture, mass flux, mixture density, and jet area to determine the velocity of the jet. Table 5 shows these results. The Damhöhler number, turbulent flame speed, turbulent flame thickness, and flame volume follow, as described above. Table 6 shows their values.

Table 5, Jet Diameters, Jet Velocities, Turbulent Intensities, Mixing Times, and Chemical Times for Experiments of Horning and Malte

	CO/H2	Phi	Jet Diameter m	Jet Velocity m/s	Turbulent Intensity m/s	Mixing Time ms	Chemical Time ms
Horning	0.5	0.550	0.001	104.4	10.4	0.096	0.015
	1	0.540	0.001	104.5	10.5	0.096	0.023
	1.27	0.536	0.001	104.3	10.4	0.096	0.025
	1.69	0.532	0.001	103.9	10.4	0.096	0.028
	2.05	0.529	0.001	103.6	10.4	0.097	0.030
	2.56	0.526	0.001	103.2	10.3	0.097	0.031
	3.2	0.524	0.001	102.8	10.3	0.097	0.032
Malte	0.33	0.661	0.0056	182.4	18.2	0.307	0.139
	1	0.625	0.0056	186.1	18.6	0.301	0.185
	3	0.628	0.0056	189.0	18.9	0.296	0.184

Table 6, Damköhler Numbers, Turbulent Flame Speeds, Flame Thicknesses, Flame Volumes, and Flame Volume Percentages for Experiments of Horning and Malte

	CO/H2	Phi	Da	ST, m/s	Flame Thickness mm	Flame Volume mm^3	Flame Percent of Reactor %
Horning	0.5	0.550	6.2	10.8	0.96	14.0	0.70
	1	0.540	4.2	10.7	0.98	14.6	0.73
	1.27	0.536	3.8	10.6	0.98	14.9	0.74
	1.69	0.532	3.5	10.5	0.99	15.1	0.75
	2.05	0.529	3.3	10.5	0.99	15.2	0.76
	2.56	0.526	3.2	10.4	0.99	15.3	0.77
	3.2	0.524	3.1	10.4	0.99	15.4	0.77
Malte	0.33	0.661	2.2	18.0	5.69	2888	4.51
	1	0.625	1.6	17.7	5.90	3227	5.04
	3	0.628	1.6	17.9	5.91	3249	5.08

Comparing the volume of the flame, determined using the calculated flame speeds of the fuel-air mixtures, to the overall reactor volume is a useful guideline for determining the size of the first PSR in the chemical reactor model. Table 6 shows that when modeling the 6.5 atm experiments, the first element should be about 0.75% of the reactor volume. Modeling of the 1 atm experiments should use a first element of 5% of the reactor volume. For these experimental conditions, the Damköhler number is relatively large.

Therefore, the turbulent flame speed is near its limiting value of $S_L + u'$. Since the turbulent flame speed is much larger than the laminar flame speed, the turbulent flame speed is about equal to u'. This simplifies the calculation of the turbulent flame thickness to $\delta_T \approx d_o$. The experiments of Horning and Malte use inlet jet diameters of 1 mm and 5.6 mm, respectively. In Section 4, these results are compared to the PSB elements sizes of the modeling of both experiments.

Equivalence Ratio Influence on NO_x Prediction

In preliminary analysis of Horning's NO_x data, the Φ calculated from the combustion products did not vary smoothly with the molar ratio of the fuel. This is shown in Figure 5. Inaccurate calculation of Φ for a given set of conditions can result from recording experimental measurements too quickly, before the JSR and meters have stabilized.

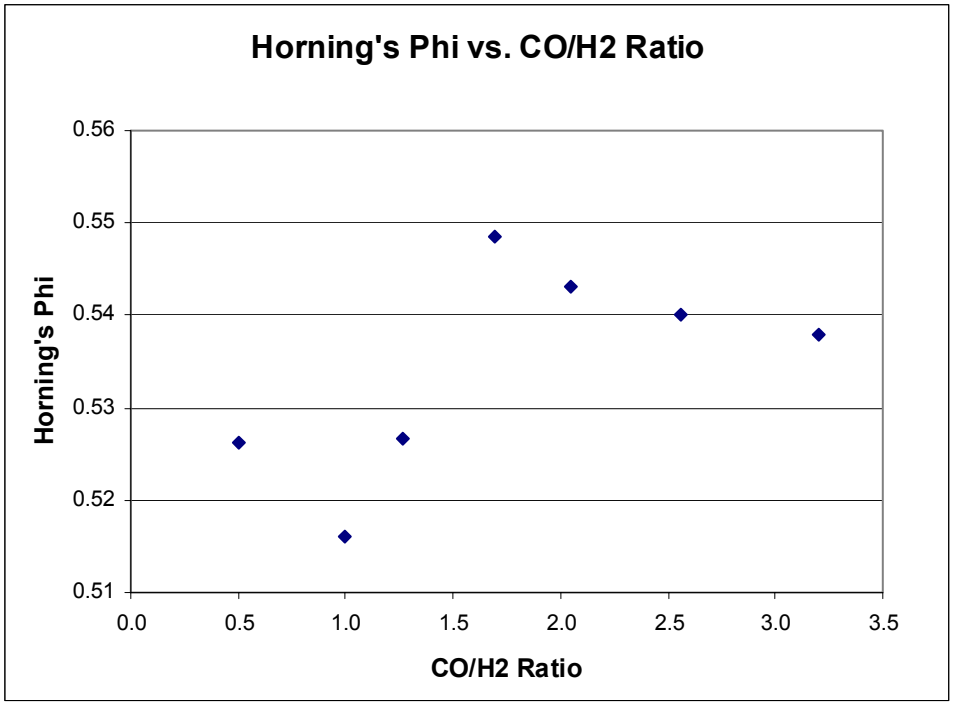

Figure 5, Horning's Φ Varying with Fuel Molar Ratio

As shown by Figure 5, while the lowest and highest molar ratios have similar Φ, there is an abrupt jump between molar ratios of 1.0 and 2.0. This lack of smoothness may affect NO_x predictions. Using a PSB+PST configuration to model the JSR, Figure 6 shows the sensitivity of NO_x to small changes in Φ for $CO/H_2 = 1.69$.

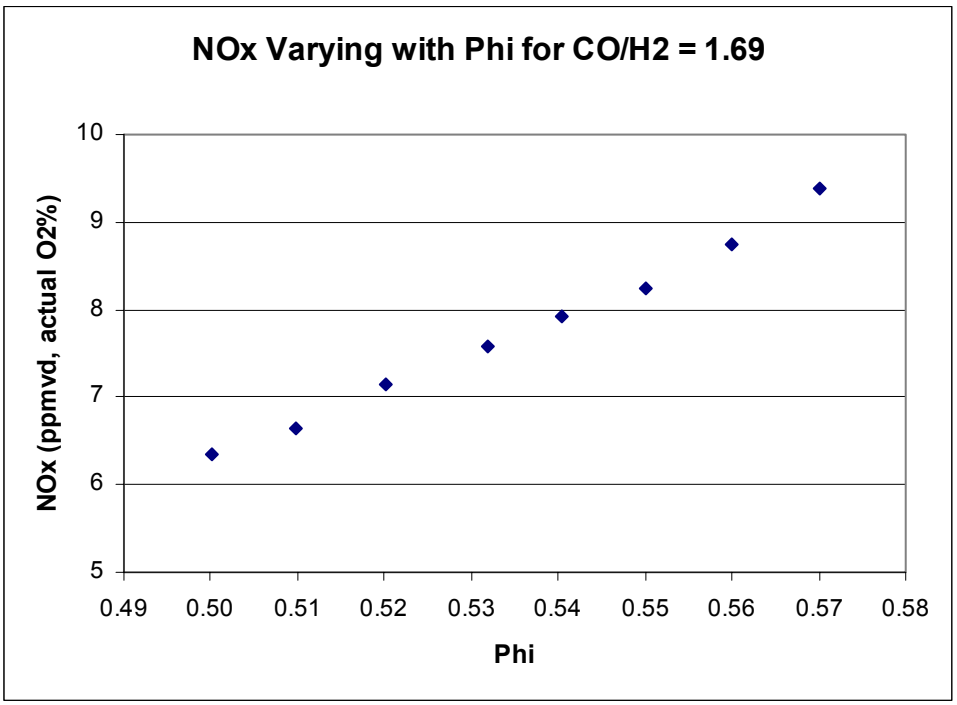

Figure 6, Sensitivity of NO_x to Φ

As indicated by Figure 6, Horning's Φ measurements of 0.52-0.55 could affect the NO_x prediction by at least 1 ppm. For nominal NO_x levels of 5-10 ppm, this is a significant variation. Because temperature measurements are more reliable than the calculations of Φ based on rotometer and product gas measurements, the model is used to determine the Φ necessary for an adiabatic equilibrium temperature of 1785 K for each molar ratio. Figure 7 shows these results.

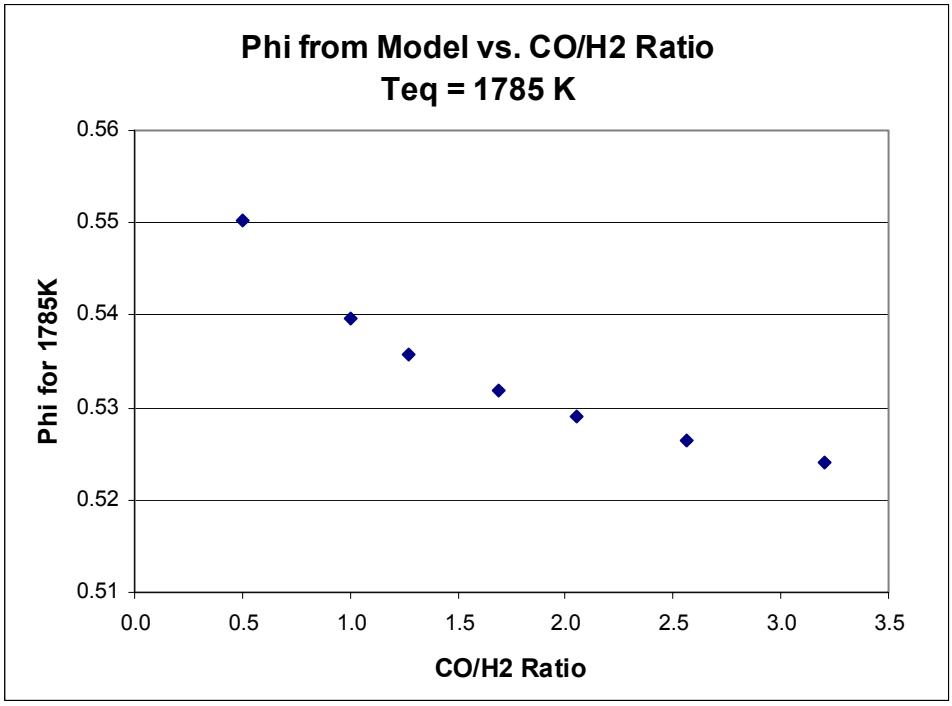

Figure 7, Φ Given by Model for Teq = 1785 K

The Φ values determined by the model for T_{eq} = 1785 K decrease smoothly with CO/H_2 ratio. Thus, as the fuel mixture contains more CO, a combustion temperature of 1785 K is obtained using leaner Φ. For all subsequent modeling of Horning's data, the Φ required to obtain an adiabatic equilibrium temperature of 1785 K is used.

Predicting Carbon Monoxide Concentrations with Modeling

Previous modeling has suggested that a short plug-flow reactor (PFR) is necessary to match experimental CO concentrations.[8,10] A PFR or a PFT – a PFR at assigned temperature, accounts for oxidation that occurs in the JSR recirculation zone and in the sampling probe by allowing greater relaxation of CO toward equilibrium than does the stirred nature of a PSR. Addition of a PFT reactor allows predicted concentrations of CO to decrease, thus better matching experimental values, while leaving NO_x predictions virtually unchanged. Figure 8 shows Horning's 6.5 atm experimental CO concentrations

with the model predictions. The model uses the PSB+PST configuration described above, with the addition of various sizes of PFT. In each case, the additional volume added by the PFT is subtracted from the volume of the large PST to keep the overall reactor volume and residence time constant.

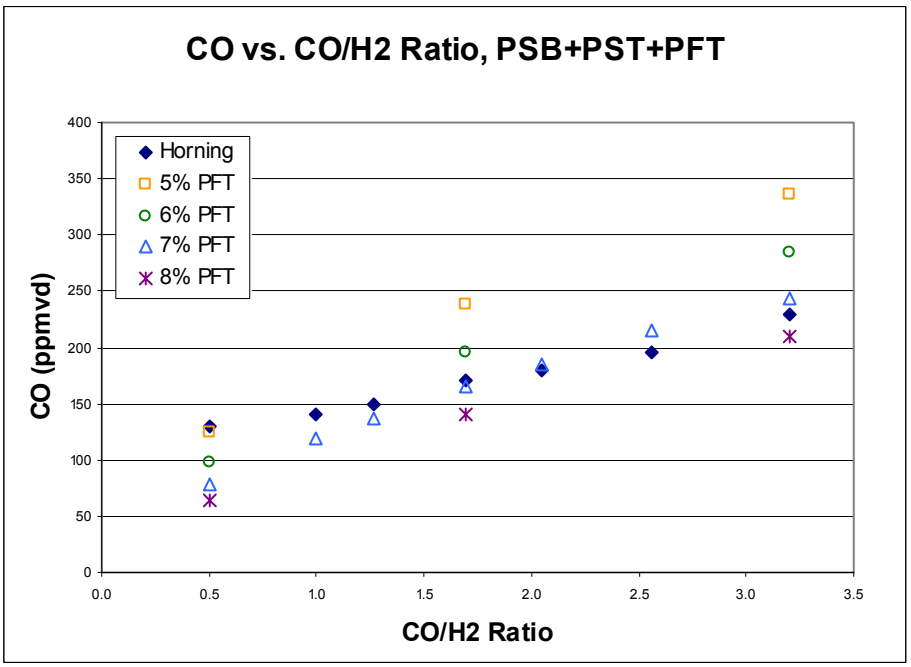

Figure 8, CO Varying with Fuel Molar Ratio for Various PFT Sizes

The configuration using a 7% PFT matches Horning's CO data and its slope best. Therefore, the following modeling of Horning's and Malte's data incorporates this size PFT, using a PSB+PST+ PFT(7%) configuration.

Section 4: Comparison of Mechanisms by NO_x Prediction

GRI 3.0 Mechanism

The GRI 3.0 chemical kinetic mechanism has been used successfully to model and predict NO_x in methane combustion.[5] It has not, however, been shown to effectively model CO/H_2 combustion. Figure 9 shows the NO_x predicted by GRI 3.0 for Horning's 6.5 atm experiments. In the PSB+PST+PFT(7%) configuration, the PSB element is adiabatic; the PST and PFT elements are assigned the experimentally-measured temperature.

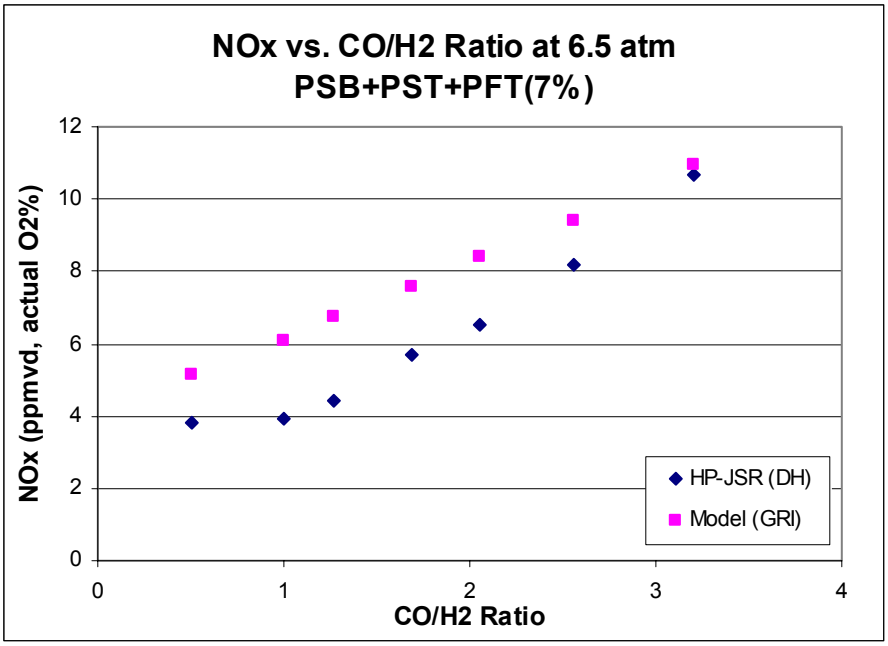

Figure 9, GRI 3.0 NO_x Predictions at 6.5 atm

At high pressure, the mechanism models the measured NO_x well at the highest fuel molar ratio. The modeling does not follow the overall trend in the data, though, over predicting by more than 2 ppm at CO/H_2 ratios near 1. Figure 10 shows the GRI 3.0 predictions for 1 atm. In the preliminary modeling, only the lowest fuel and air preheat temperature data, $T_i = 423$ K, is analyzed.

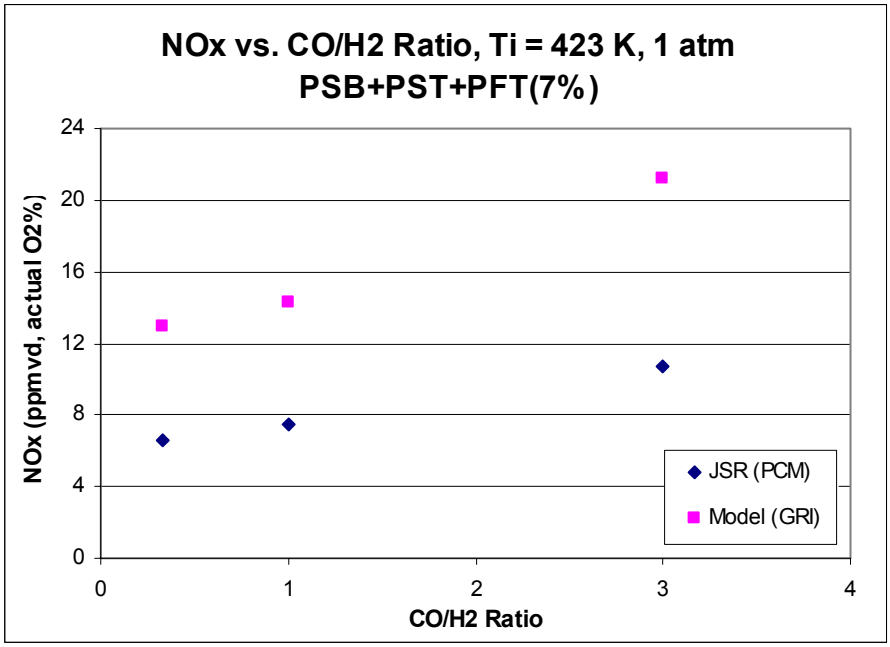

Figure 10, GRI 3.0 NO_x Predictions at T_i = 423 K and 1 atm

The atmospheric pressure predictions of NO_x by GRI 3.0 do not agree with the measurements. For all molar ratios, the mechanism predicts NO_x concentrations about twice those measured by experiment.

UCSD Mechanism

The next mechanism tested is that developed by Forman Williams at UCSD.[15] This mechanism includes both CO/H_2 oxidation chemistry (24 reactions) and nitrogen chemistry (52 reactions). Thus far, the nitrogen chemistry of this mechanism has not been thoroughly tested. Though not included in the UCSD mechanism, the following two reactions are included in the present modeling, for completeness, along with their corresponding GRI 3.0 rate constants:

$$O + CO + M = CO_2 + M$$

$$O_2 + CO = O + CO_2$$

Figure 11 shows the NO_x predicted by the UCSD mechanism at 6.5 atm.

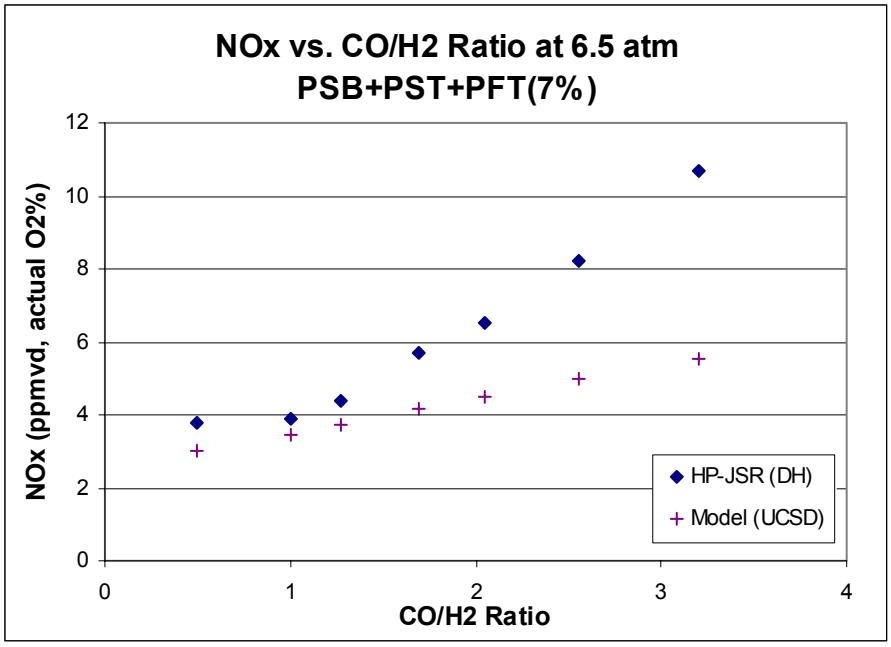

Figure 11, UCSD NO_x Predictions at 6.5 atm

The NO_x predictions of the UCSD mechanism match well with measurements at low CO/H_2 ratios. But, the mechanism predictions do not show the same slope as the measurements and under predict by about a factor of two at high fuel molar ratios. Figure 12 shows the UCSD NO_x predictions for 423 K and 1 atm.

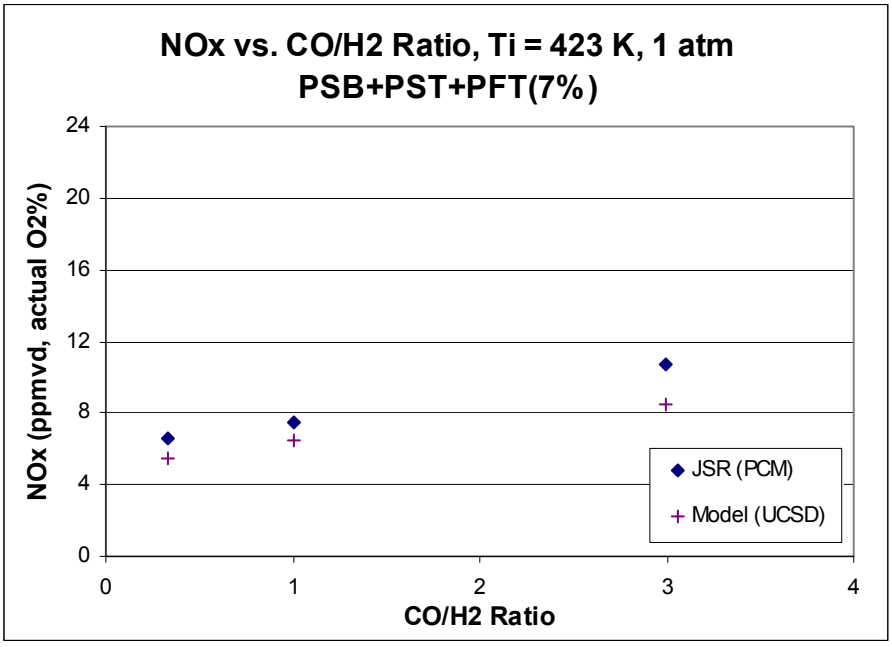

Figure 12, UCSD NO_x Predictions at T_i = 423K and 1 atm

The UCSD mechanism is within 2.2 ppm at all molar ratios. As with the modeling at 6.5 atm, the under prediction of NO_x is more apparent at high CO/H_2 ratios. The model results from the GRI 3.0 and UCSD mechanisms differ significantly. To determine whether the CO/H_2 chemistry, the nitrogen chemistry, or both accounted for the difference in NO_x prediction, the nitrogen chemistry from GRI is combined with CO/H_2 chemistry from UCSD, and vice versa. These two new combination mechanisms are used to model the same experimental data. Figure 13 shows modeling of the two new mechanisms and the GRI and UCSD parent mechanisms, along with the high pressure data.

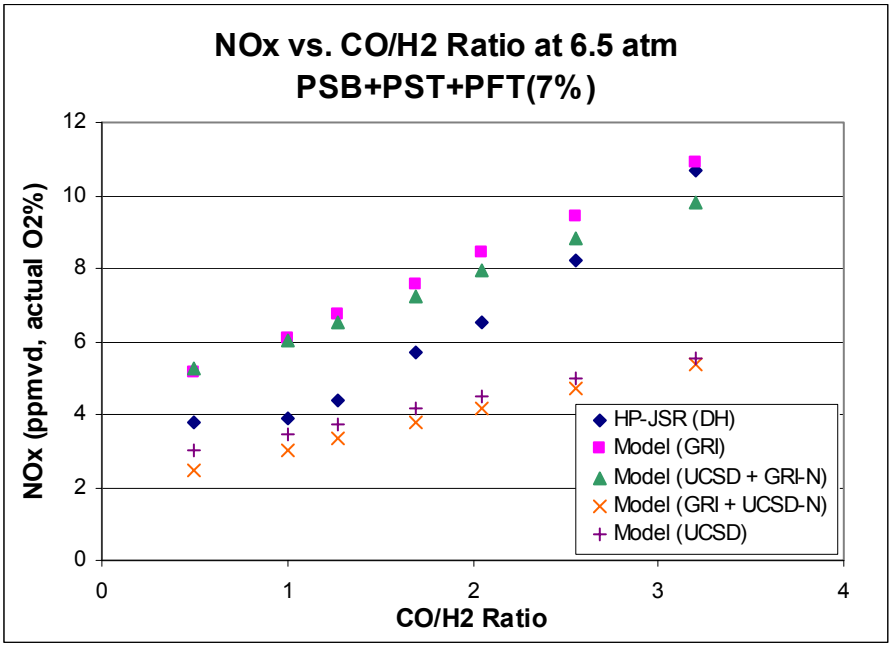

Figure 13, GRI, UCSD, and Combination NO_x Predictions at 6.5 atm

Predictions of NO_x by the complete GRI 3.0 mechanism and the UCSD (CO/H_2) + GRI 3.0 (nitrogen) mechanism are very similar. This is also the case when the complete UCSD mechanism and the GRI 3.0 (CO/H_2) + UCSD (nitrogen) mechanism are compared. Therefore, the majority of the difference in NO_x predictions of the GRI 3.0 and UCSD mechanisms results from the nitrogen chemistry, not the CO/H_2 chemistry. Figure 13 also shows that at mid-range fuel molar ratios, the UCSD mechanism under predicts NO_x by about as much as GRI over predicts. The UCSD mechanism is more accurate at low CO/H_2 ratios; GRI 3.0 is more accurate at high molar ratios. Figure 14 shows the predictions by all four mechanisms for 423 K inlet temperature and 1 atm.

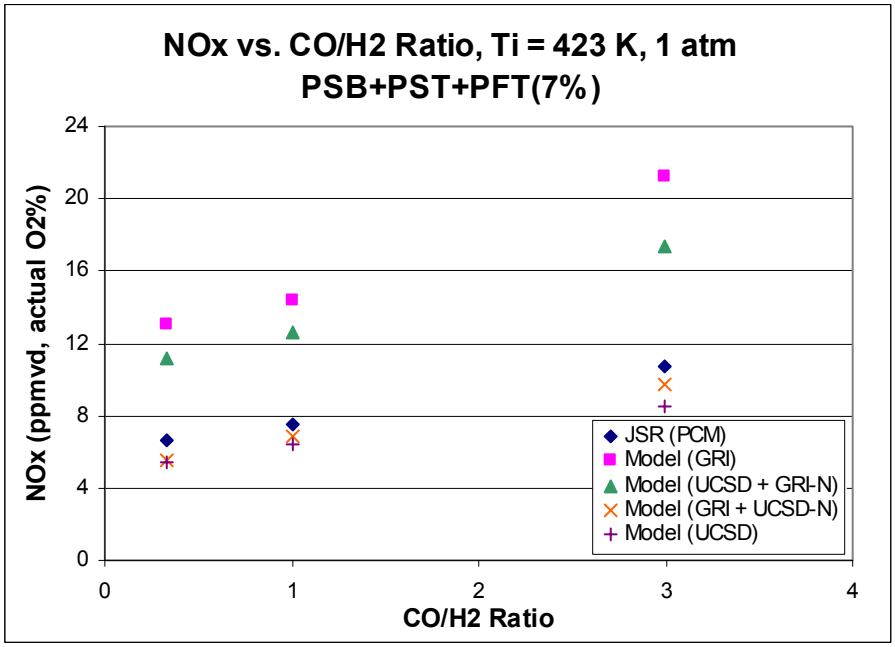

Figure 14, GRI, UCSD, and Combination NO_x Predictions at T_i = 423 K and 1 atm

It is also apparent at 1 atm that the nitrogen chemistry constitutes the majority of the difference in NO_x prediction between GRI 3.0 and UCSD. The slope of the experimental NO_x measurements at 1 atm, however, has a much more gradual slope than do the measurements at 6.5 atm. The UCSD mechanism matches the measurements well over the entire range of fuels at 1 atm. The UCSD mechanism, however, is not accurate at conditions of high pressure combined with high CO/H_2 fuel ratio; a more robust mechanism is needed.

Modified Tomeczek and Gradoń Mechanism

The final mechanism employed is from the work of Tomeczek and Gradoń of Silesian Technical University, Poland.[16] The nitrogen chemistry of Tomeczek and Gradoń (67 reactions), with a few exceptions, is combined with GRI 3.0 CO/H_2 chemistry (30 reactions), to obtain the mechanism tested. Tomeczek and Gradoń used the rate constant for $N_2O+M=N_2+O+M$ from a study done at 1000-1400 K by Glarborg et al.[17] Glarborg

et al. suggest using the rate constant of Michael and Lim[18] for higher temperatures. For this reaction, this thesis uses the rate constant of Michael and Lim, which is valid up to 2500 K. Finally, because the rate of Michael and Lim for $N_2O+M=N_2+O+M$ does not incorporate the pressure dependence of this reaction, the GRI rate constant for high pressure is used along with the rate constant of Michael and Lim in the modified mechanism. The effective rate constant for this reaction is a function of both the low-pressure and high-pressure rate constants.

Rate constants for:

$$N_2 + O = NO + N$$
$$N_2O + O = NO + NO$$
$$N_2O + O = N_2 + O_2$$

were taken by Tomeczek and Gradoń from their previous work investigating N_2O formation using a mixture of oxygen and nitrogen in a tubular flow reactor.[19] This work also showed that N_2O formation depended heavily on the presence of hydrogen in the mixture. Tomeczek and Gradoń suggested substantial enhancements of these rate constants to match the high N_2O concentrations of their experiments using hydrogen-free fuel. These increased rate constants, however, lead to a large over prediction of NO_x in the combustion of H_2-containing fuels.[19] Over prediction of NO_x for the CO/H_2 fuels in this thesis was found to be an order of magnitude over experimental NO_x values. Because the rate constants of Tomeczek and Gradoń for the three reactions above are not applicable to this study of CO/H_2 combustion, those rate constants were replaced by the GRI 3.0 rates. Appendix B shows the modified version of the Tomeczek and Gradoń mechanism used here.

Figure 15 shows the NO_x predictions of the modified Tomeczek and Gradoń mechanism with the previous results at 6.5 atm.

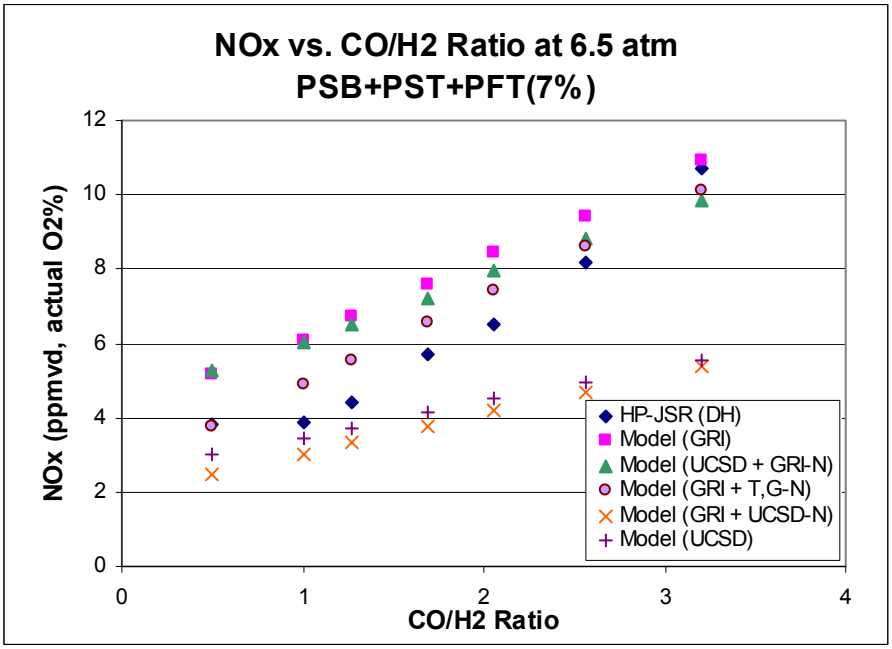

Figure 15, GRI, UCSD, and Modified Tomeczek and Gradoń NO_x Predictions at 6.5 atm

The NO_x predicted by the modified Tomeczek and Gradoń mechanism follows the slope of Horning's experimental data very well. It matches the data almost exactly at both the high and the low ends of the fuel range and differs from Horning's data by 1.13 ppm or less over the entire range. Table 7 gives the exact results of Figure 15.

Table 7, GRI, UCSD, and Modified Tomeczek and Gradoń NO_x Predictions at 6.5 atm

	NOx (ppmvd, actual O2%)					
CO/H2	**Horning**	**GRI 3.0**	**UCSD + GRI-N**	**GRI + UCSD-N**	**UCSD**	**GRI + T,G-N**
0.5	3.80	5.14	5.26	2.48	3.02	3.78
1	3.90	6.10	6.03	3.02	3.46	4.89
1.27	4.40	6.75	6.53	3.32	3.71	5.53
1.69	5.70	7.58	7.23	3.78	4.15	6.55
2.05	6.50	8.42	7.96	4.17	4.49	7.41
2.56	8.20	9.40	8.81	4.71	4.97	8.62
3.2	10.70	10.92	9.83	5.38	5.55	10.10

Figure 16 shows the CO concentrations predicted by the modified Tomeczek and Gradoń mechanism for Horning's data.

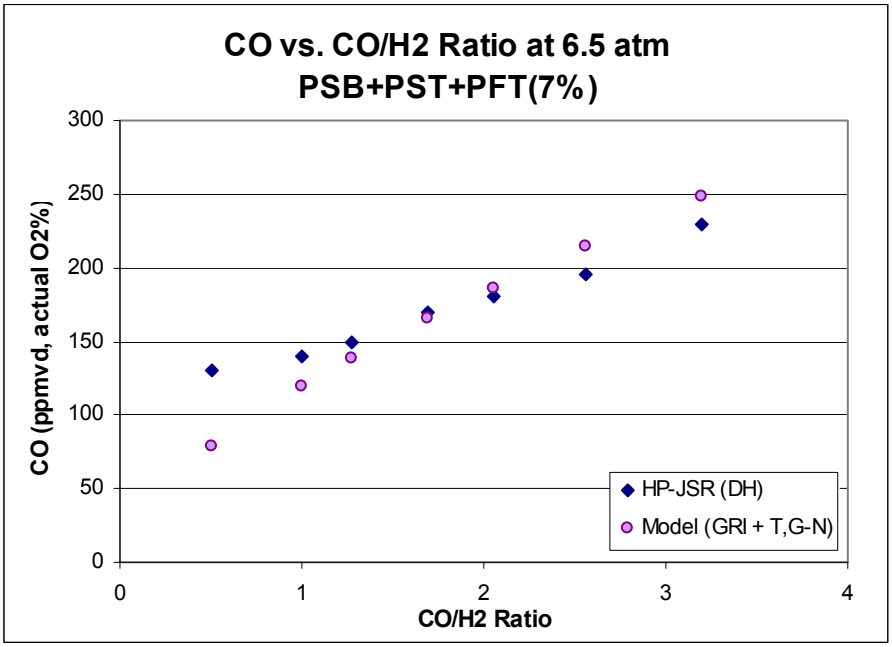

Figure 16, Modified Tomeczek and Gradoń CO Predictions at 6.5 atm

Since the modified Tomeczek and Gradoń mechanism uses GRI 3.0 CO/H_2 chemistry, its CO predictions are very close to those of GRI 3.0 in Figure 10 for a 7% PFT. Although the modified Tomeczek and Gradoń mechanism under predicts by about 50 ppm for the lowest CO/H_2 case, its predictions are a good overall fit for the data.

As a final check of the modified Tomeczek and Gradoń mechanism at high pressure, the length of the PSB is compared to the calculated flame volume percentage. Table 8 shows this check.

Table 8, Calculated and PSB Flame Volume Percentages at 6.5 atm

CO/H2	Phi	Flame Percent of Reactor %	PSB Percent of Reactor %
0.5	0.550	0.70	0.71
1	0.540	0.73	1.42
1.27	0.536	0.74	1.75
1.69	0.532	0.75	2.17
2.05	0.529	0.76	2.50
2.56	0.526	0.77	2.90
3.2	0.524	0.77	3.34

As Table 8 shows, the PSB volume is at least as great as the calculated flame zone volume in each case. At the lowest fuel molar ratio the volume percentages are about equal. As the fuel mixtures contain more CO and less H_2, however, the PSB element in the model requires a larger volume for convergence. The flame volume percentage calculation fails to show sensitivity to CO/H_2 ratio because the relatively high Damköhler numbers (3.1 to 6.2), lead to the limiting value of $S_T = u'$ in all cases. This results in little change in the calculation of δ_T and the flame volume percentage. Because the blowout volume found using the PSB model increases with increasing CO/H_2 ratio, except for the high H_2 fuel, it is impossible to run the first element near 0.7% of the reactor volume. Therefore, the PSB+PST+PFT(7%) configuration is not modified.

Next, the predictions of all the mechanisms are compared to the measurements at 1 atm. Figure 17 shows the predictions for 1 atm and $T_i = 423$ K.

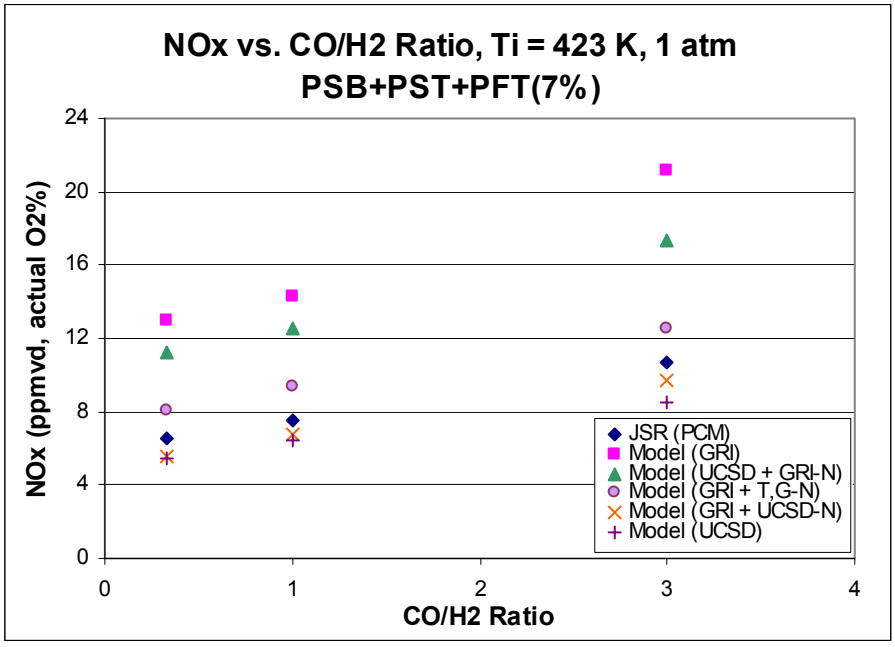

Figure 17, GRI, UCSD, and Modified Tomeczek and Gradoń
NO_x Predictions at T_i = 423 K and 1 atm

The modified Tomeczek and Gradoń mechanism is also in close agreement with the 1 atm measurements. The predicted NO_x concentrations are within 1.9 ppm of the measurements and show the same increasing trend as Malte's measurements. Table 9 gives the results shown in Figure 17.

Table 9, GRI, UCSD, and Modified Tomeczek and Gradoń
NO_x Predictions at T_i = 423 K and 1 atm

	NOx (ppmvd, actual O2%)					
CO/H2	Malte	GRI 3.0	UCSD + GRI-N	GRI + UCSD-N	UCSD	GRI + T,G-N
0.33	6.6	13.00	11.20	5.56	5.45	8.03
1	7.5	14.34	12.56	6.81	6.44	9.37
3	10.7	21.18	17.33	9.69	8.47	12.48

The modified Tomeczek and Gradoń mechanism, as shown by Figures 15 and 17, matches experimental NO_x data reasonably well over the entire fuel molar ratio range, for both 1 atm and 6.5 atm. While the UCSD mechanism predicts experimental

measurements about as closely as the modified Tomeczek and Gradoń mechanism at 1 atm, it does not predict as well at high pressure. Overall, the NO_x predictions of the modified Tomeczek and Gradoń mechanism agree best with the experimental measurements. Modeling the remaining preheat temperatures from Malte's experiments determines whether the mechanism is useful for varying preheat temperature. Figure 18 shows the results.

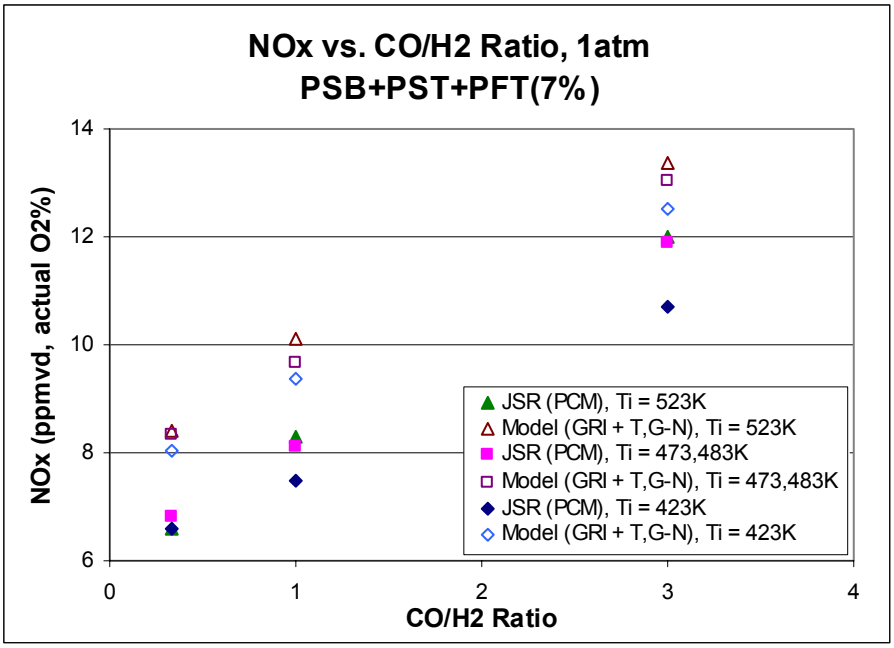

Figure 18, Modified Tomeczek and Gradoń NO_x Predictions for all Preheat Temperatures at 1 atm

The mechanism models NO_x at preheat temperatures of 473-523 K as well as it models NO_x at T_i = 423 K. For each case, the mechanism predicts NO_x levels 1.4 to 1.9 ppm higher than measured. Figure 19 shows the CO concentration predictions of the modified Tomeczek and Gradoń mechanism at 1 atm for T_i = 423 K.

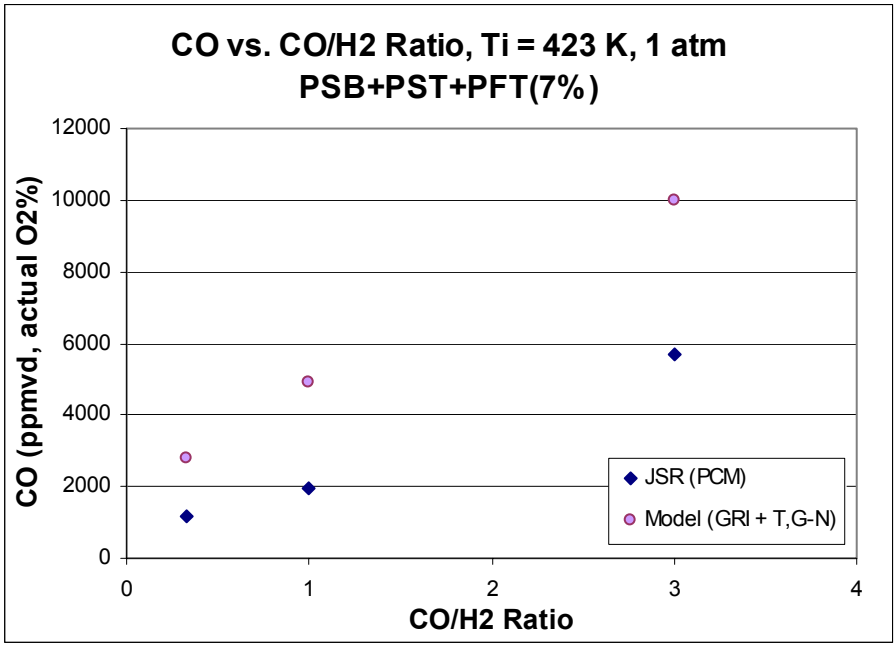

Figure 19, Modified Tomeczek and Gradoń CO Predictions at 1 atm

Figure 19 shows that the PSB+PST+PFT(7%) configuration does not model CO as effectively at 1 atm as it does at 6.5 atm. Because CO is more slowly relaxed toward equilibrium concentrations at the lower pressure, a larger PFT element is necessary to model the effect of oxidation in the JSR recirculation zone and in the sampling probe. Therefore, a change in the element configuration is needed. This is shown below.

Table 10 compares the length of the PSB element at 1 atm with the calculated values of the flame volume.

Table 10, Calculated and PSB Flame Volume Percentages at 1 atm

CO/H2	Phi	Flame Percent of Reactor %	PSB Percent of Reactor %
0.33	0.661	4.51	0.74
1	0.625	5.04	1.60
3	0.628	5.08	3.76

As shown at 6.5 atm, the flame volume percentage calculations at 1 atm show little sensitivity to CO/H_2 ratio. In this case, however, the PSB modeling results in an initial reactor size smaller than that predicted by the flame volume calculations.

In order to improve both the CO prediction and flame volume percentage of the model, three new configurations are tested. First, since the flame volume calculations indicate the flame zone is approximately 5% of the reactor, a PSR(5%)+PST+PFT(7%) configuration is used. Second, the PFT size is increased to more closely match the CO measurements. A PFT of 17.5%, or a configuration of PSR(5%)+PST+PFT(17.5%), provides adequate relaxation of the free radicals. Third, research on the atmospheric, lean-premixed combustion of hydrocarbons by Lee et al.[20] has shown that splitting the initial 5% PSR into two reactors, a PSB followed by a small PSR, has been successful. In this case, the PSR has 5% of the volume, less the size of the PSB, as in PSB+PSR(<5%)+ PST+PFT(17.5%). This configuration may accurately model the flame zone by dividing the flame into two regions, one being the flame front and the other being composed of pockets of burning fuel behind the flame front. Figures 20 and 21 show the NO_x and CO predictions of all these configurations at 1 atm and T_i = 423 K using the modified Tomeczek and Gradoń mechanism.

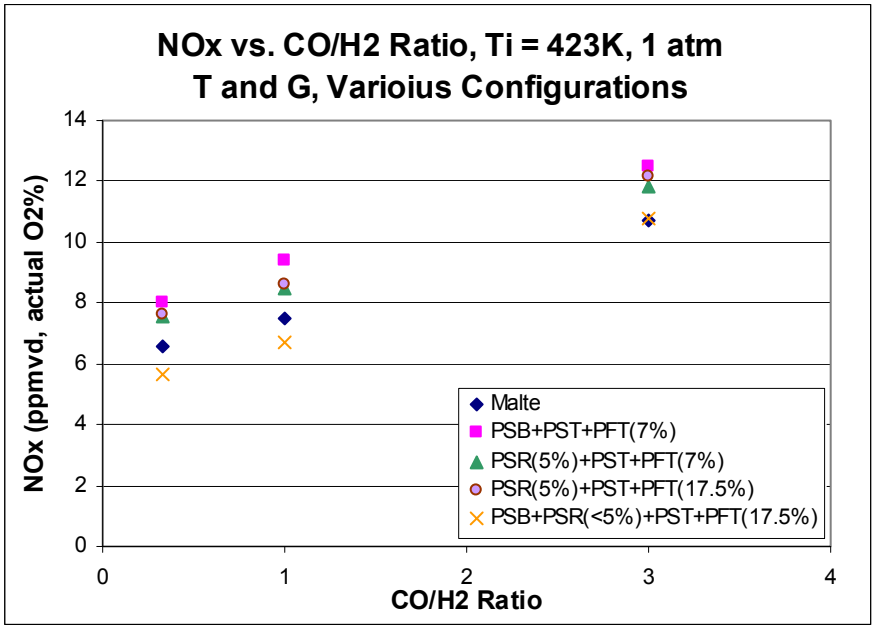

Figure 20, Modified Tomeczek and Gradoń NO_x Predictions at T_i = 423 K

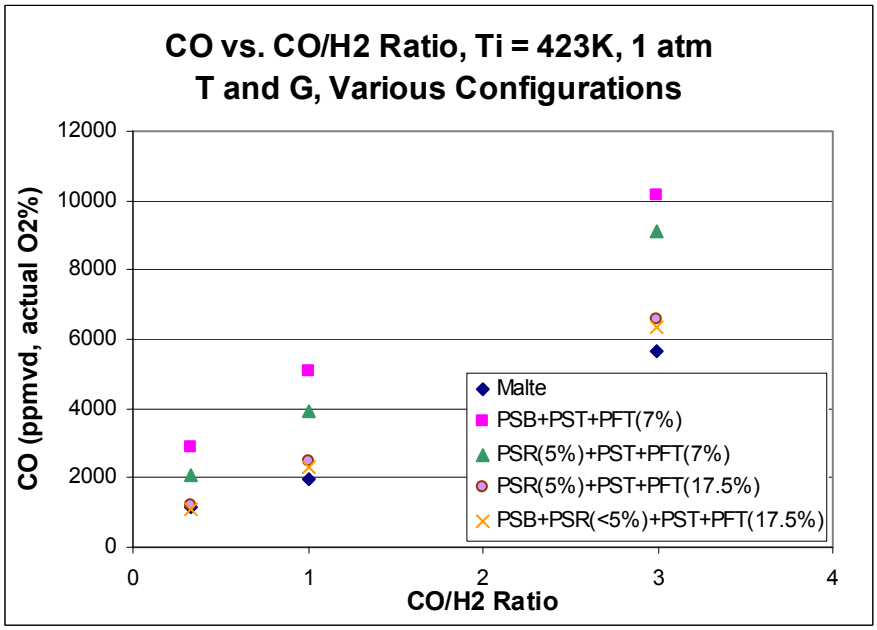

Figure 21, Modified Tomeczek and Gradoń CO Predictions at T_i = 423 K

Figure 20 shows that increasing the size of the first element decreases the NO_x prediction. Substituting two elements for the initial PSR reduces NO_x even further, to slightly below the experimental values. As expected the change in PFT size has little affect on the NO_x

prediction. The PSB+PSR(<5%)+PST+PFT(17.5%) configuration, with two initial PSR's, is the best predictor of NO_x at $CO/H_2 = 3$. But, but for the other CO/H_2 ratios, it slightly under predicts. Figure 21 confirms that the 17.5% PFR predicts the CO measurements of the experiments better than the 7% PFR does. The modeling shows that the CO predictions have very little sensitivity to the number of initial elements in the configuration. Table 11 summarizes the NO_x and CO predictions of the PSR(5%)+PST+ PFT(17.5%) and PSB+PSR(<5%)+PST+ PFT(17.5%) configurations for $T_i = 423$ K.

Table 11, Modified Tomeczek and Gradoń NO_x and CO Predictions at 1 atm and $T_i = 423$ K

	Malte		PSR(5%)+PST+PFT(17.5%)		PSB+PSR(<5%)+PST+PFT(17.5%)	
CO/H2	**NOx**	**CO**	**NOx**	**CO**	**NOx**	**CO**
0.33	6.6	1173	7.64	1211	5.68	1106
1	7.5	1969	8.62	2472	6.69	2286
3	10.7	5681	12.15	6559	10.79	6326

Figures 22 and 23 show the NO_x and CO predictions at $T_i = 473$-483 K.

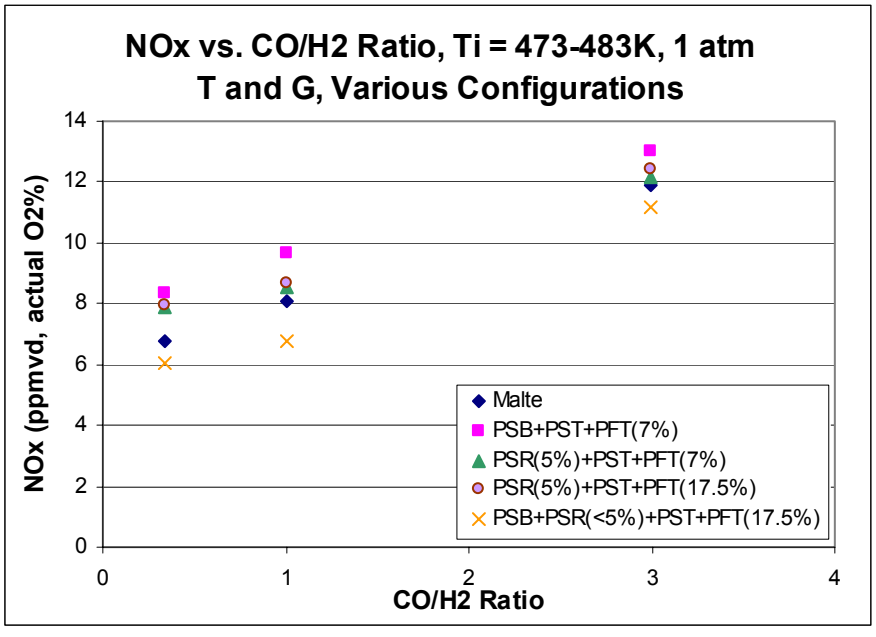

Figure 22, Modified Tomeczek and Gradoń NO_x Predictions at $T_i = 473$-483 K

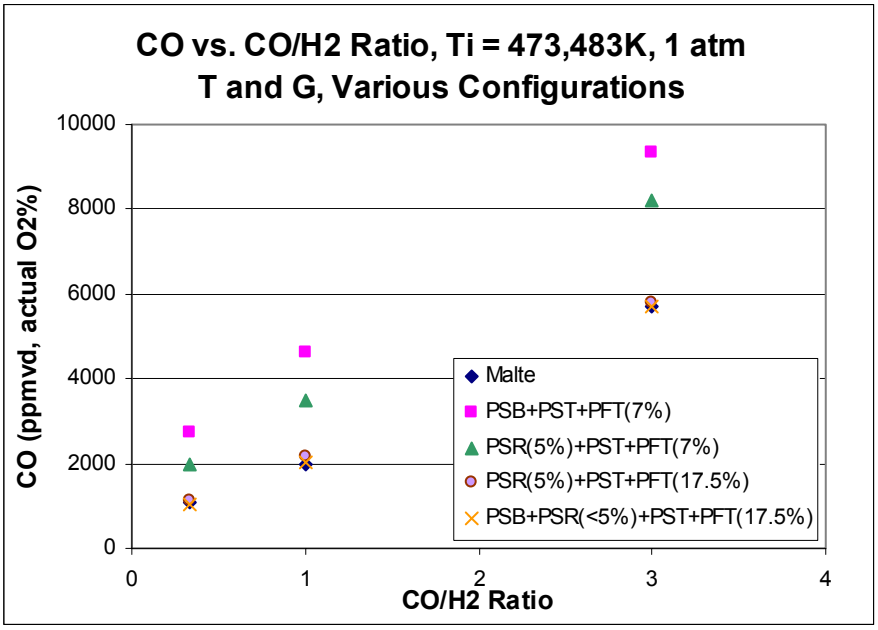

Figure 23, Modified Tomeczek and Gradoń CO Predictions at T_i = 473-483 K

For a slightly higher preheat temperature, as shown by Figure 22, the PSR(5%)+PST+ PFT(17.5%) configuration predictions agree best with the NO_x measurements. Both configurations with 17.5% PFT's predict CO very well at T_i = 473-483 K. Table 12 summarizes these results.

Table 12, Modified Tomeczek and Gradoń NO_x and CO Predictions at 1 atm and T_i = 473-483K

	Malte		PSR(5%)+PST+PFT(17.5%)		PSB+PSR(<5%)+PST+PFT(17.5%)	
CO/H2	**NOx**	**CO**	**NOx**	**CO**	**NOx**	**CO**
0.33	6.8	1102	7.96	1127	6.04	1037
1	8.1	1958	8.67	2173	6.78	2017
3	11.9	5722	12.44	5823	11.18	5698

Figures 24 and 25 show the NO_x and CO predictions of the modified Tomeczek and Gradoń mechanism for T_i = 523K.

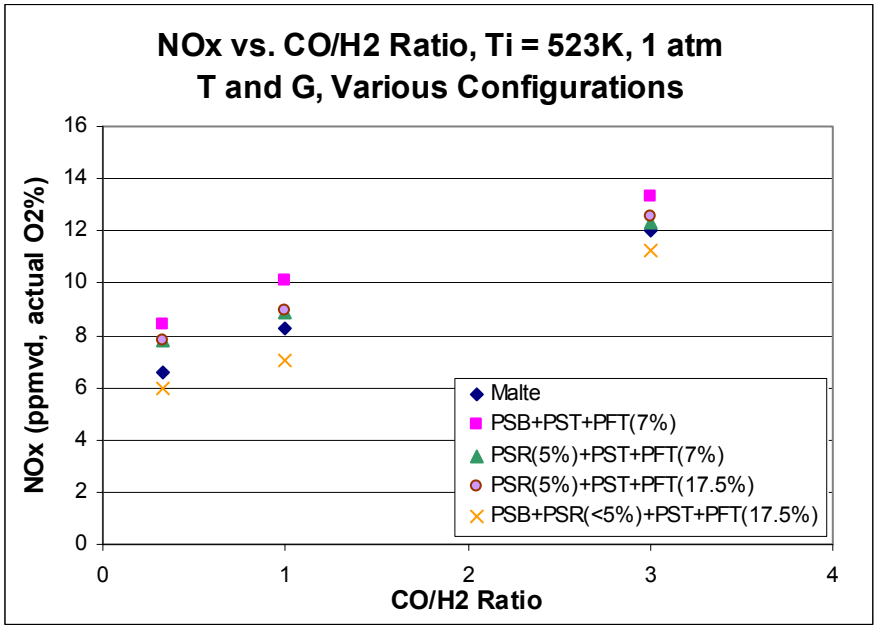

Figure 24, Modified Tomeczek and Gradoń NO_x Predictions at T_i = 523 K

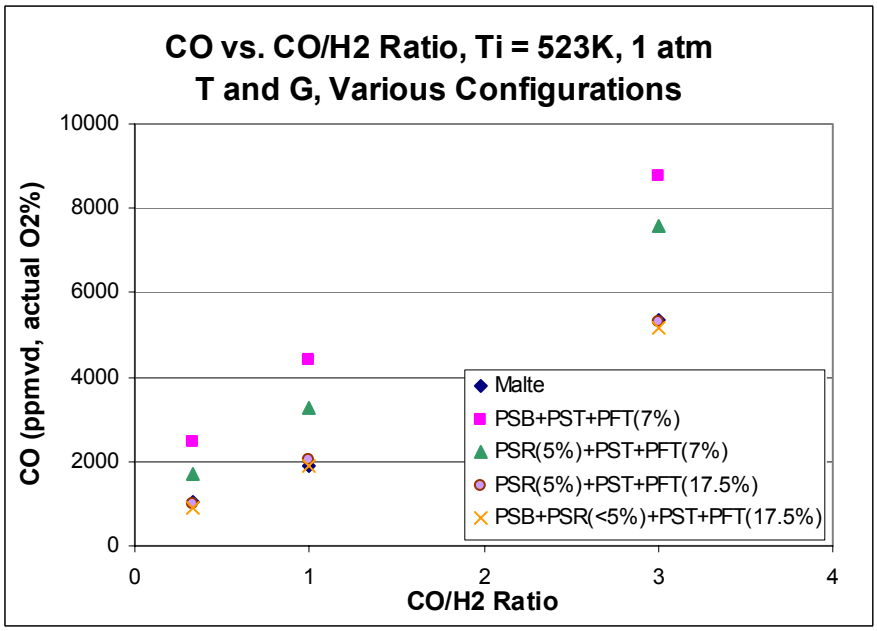

Figure 25, Modified Tomeczek and Gradoń CO Predictions at T_i = 523 K

At T_i = 523 K, the PSR(5%)+PST+PFT(17.5%) configuration predicts NO_x slightly better at higher fuel molar ratios, but the PSB+PSR(<5%)+PST+PFT(17.5%) configuration predicts slightly better at lower fuel molar ratios. Again, both of these

configurations predict CO equally well. Table 13 shows the exact NO_x and CO predictions.

Table 13, Modified Tomeczek and Gradoń NO_x and CO Predictions at 1 atm and 523 K

	Malte		PSR(5%)+PST+PFT(17.5%)		PSB+PSR(<5%)+PST+PFT(17.5%)	
CO/H2	**NOx**	**CO**	**NOx**	**CO**	**NOx**	**CO**
0.33	6.6	1061	7.74	1014	5.86	933
1	8.3	1908	8.97	2033	7.07	1892
3	12	5335	12.58	5286	11.29	5184

Overall, using the PSB+PSR(<5%)+PST+PFT(17.5%) configuration does not have any advantage over the PSR(5%)+PST+PFT(17.5%) configuration. At all fuel molar ratios and inlet temperatures, the both of these configuration predict NO_x within 1.5 ppm and CO within about a few hundred ppm. So, using initial PSR and final PFT sizes commensurate with the reactor pressure, the modified Tomeczek and Gradoń mechanism predicts measurements well at both 1 atm and 6.5 atm.

Section 5: Comparison of Mechanisms Using NO_x Formation Pathways

Nodal Diagrams

The previous section shows that the GRI 3.0, UCSD, and modified Tomeczek and Gradoń mechanisms predict quite different concentrations of NO_x in CO/H_2 combustion. In order to understand which NO_x pathways contribute to this difference, nodal diagrams are constructed for the PSB and PST elements of each mechanism at 6.5 atm and CO/H_2 = 1.69. The figures show the paths of destruction only, for each species. The paths lead from N_2 to NO, and show by percentage, the contribution of each reaction to the loss of the nodal species. The percentages for each nodal species sum to 100%, except in a few cases where very small contributions of some reactions are excluded (combined, less than 2%). Figures 26 and 27, respectively, show the nodal diagrams for the PSB (termed Element #1) and the PST (termed Element #2) elements using the GRI 3.0 mechanism. Figures 28 and 29 show those for UCSD; Figures 30 and 31 show those for the modified Tomeczek and Gradoń mechanism.

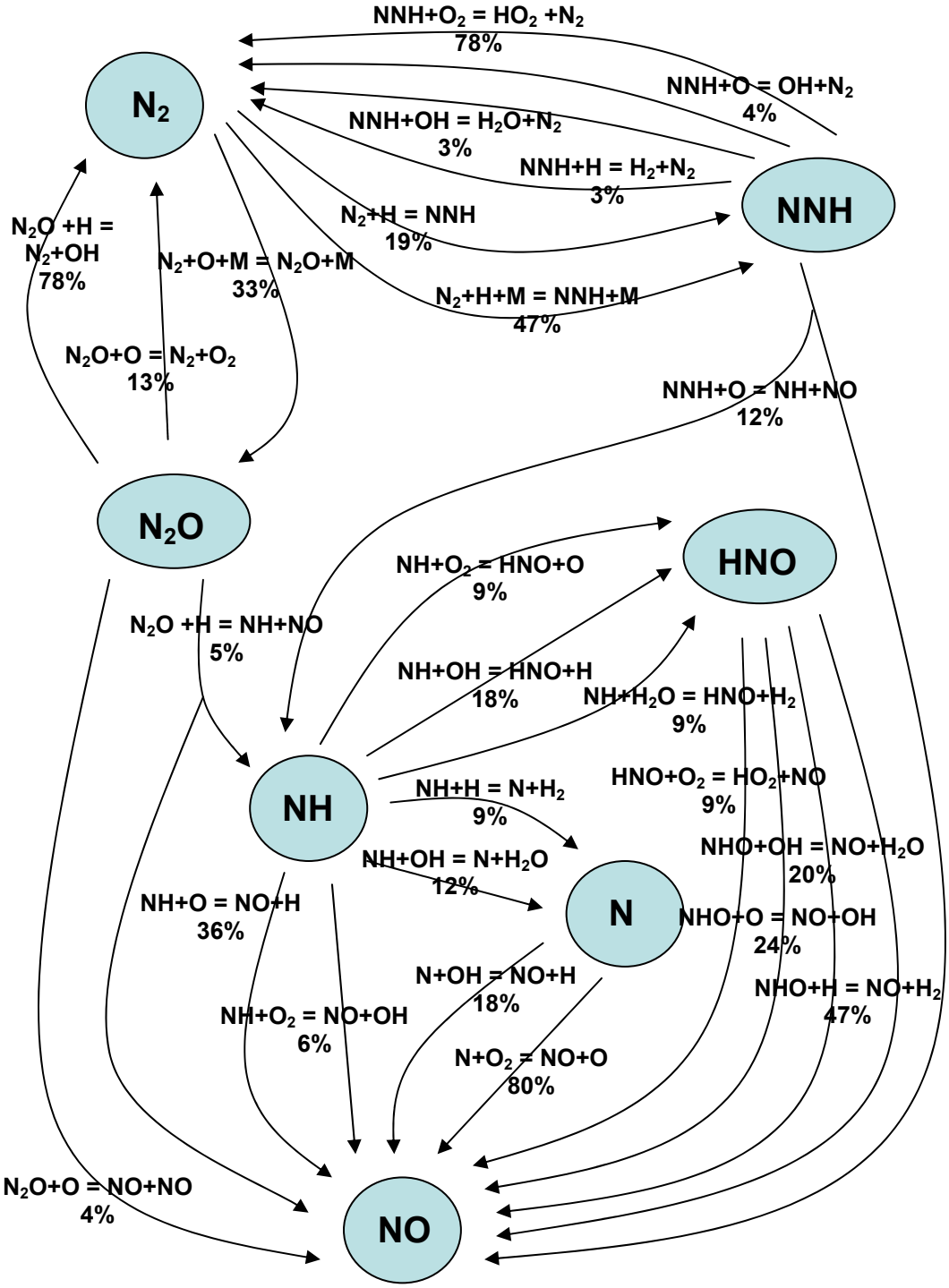

Figure 26, Nodal Diagram of Destruction to NO in PSB with GRI 3.0 Mechanism

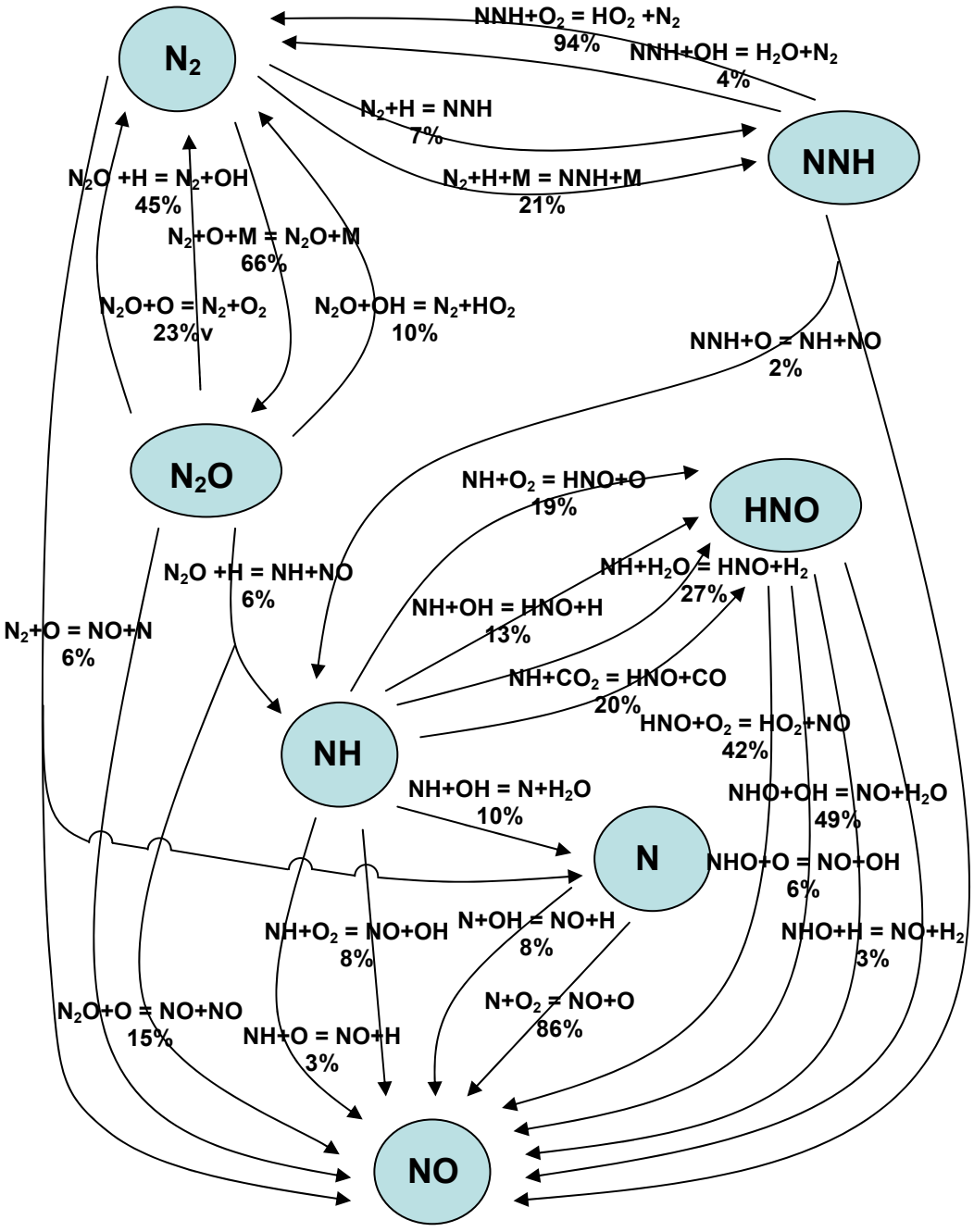

Figure 27, Nodal Diagram of Destruction to NO in PST with GRI 3.0 Mechanism

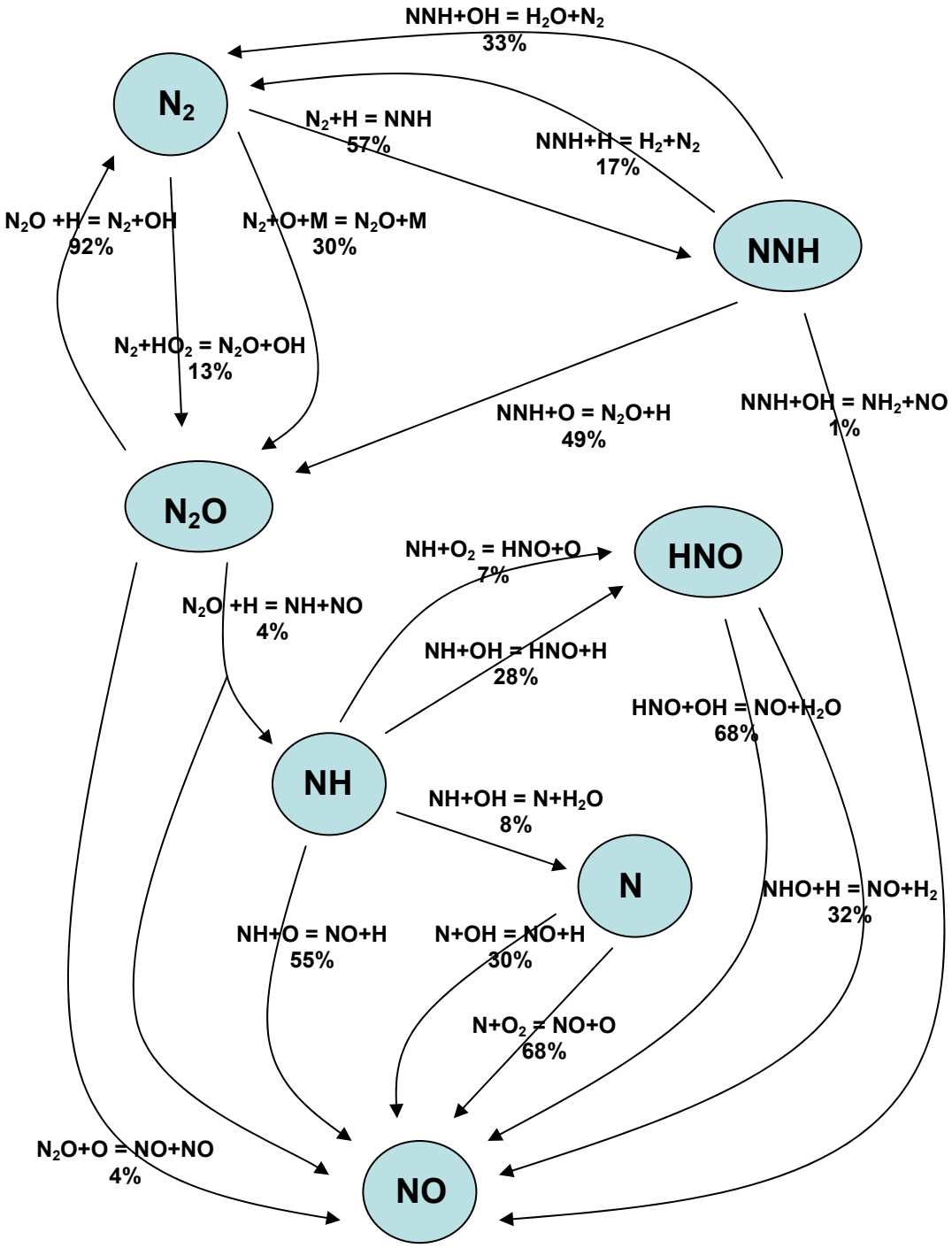

Figure 28, Nodal Diagram of Destruction to NO in PSB with UCSD Mechanism

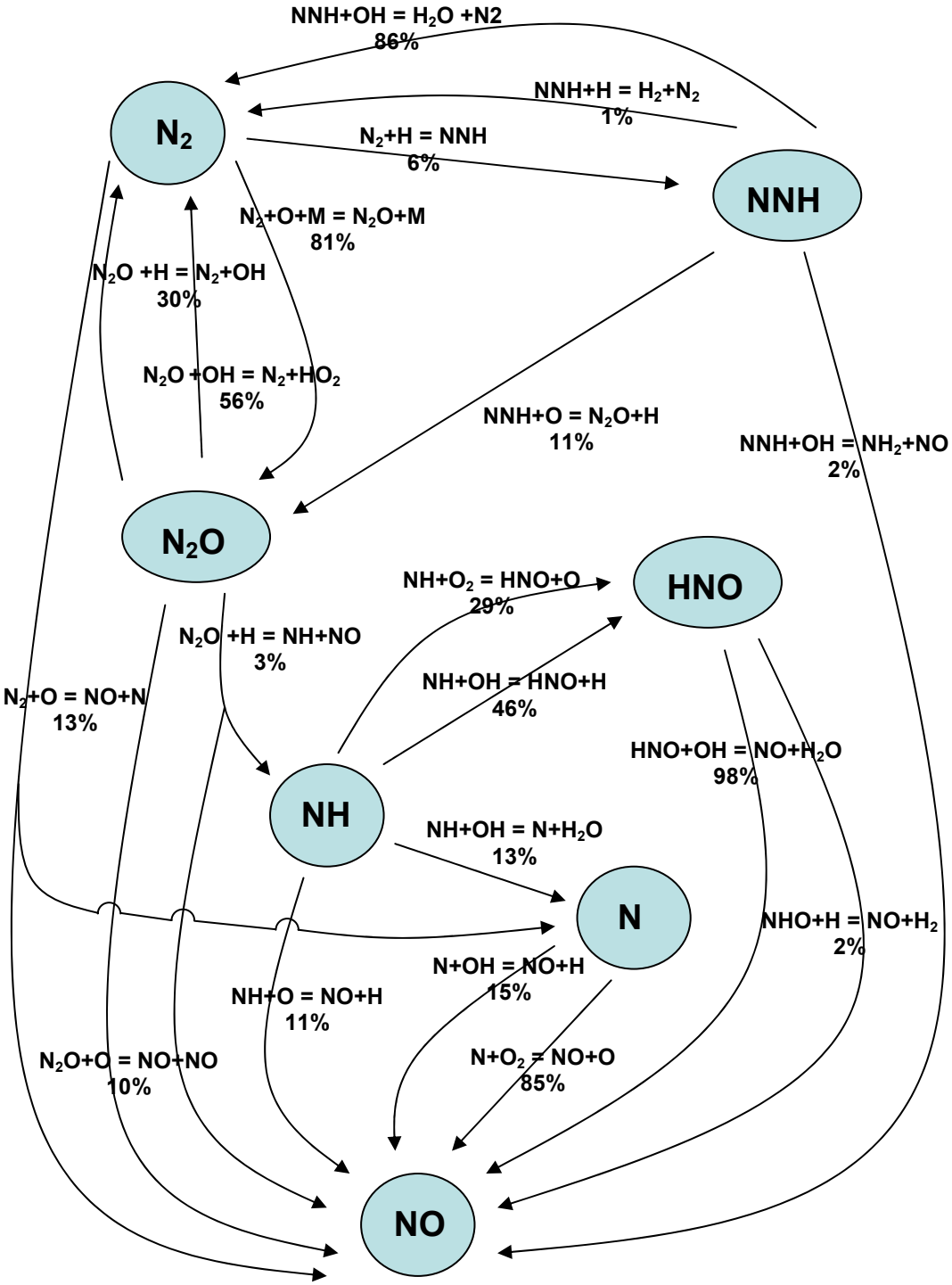

Figure 29, Nodal Diagram of Destruction to NO in PST with UCSD Mechanism

T and G Element #1

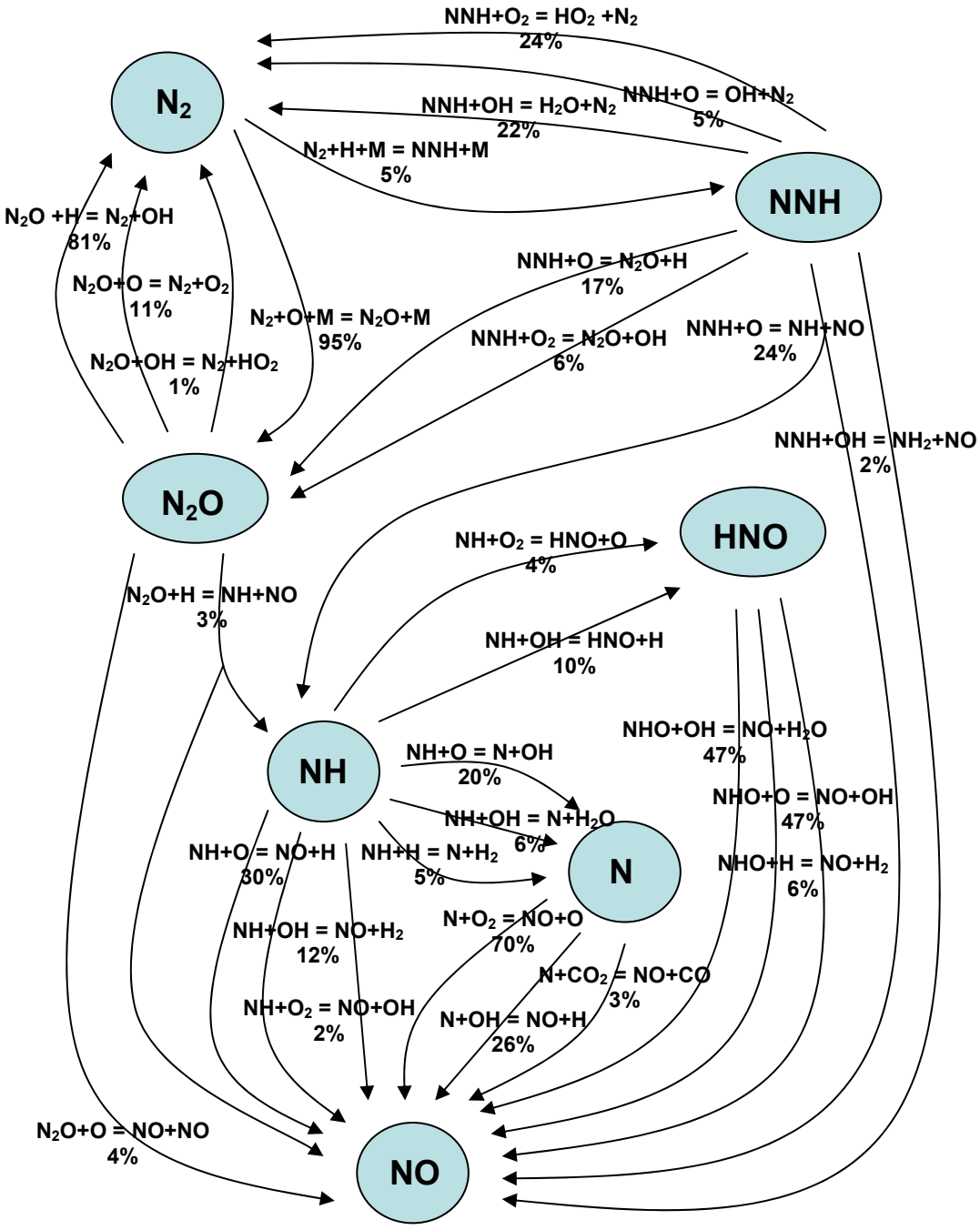

Figure 30, Nodal Diagram of Destruction to NO in PSB with Modified Tomeczek and Gradoń Mechanism

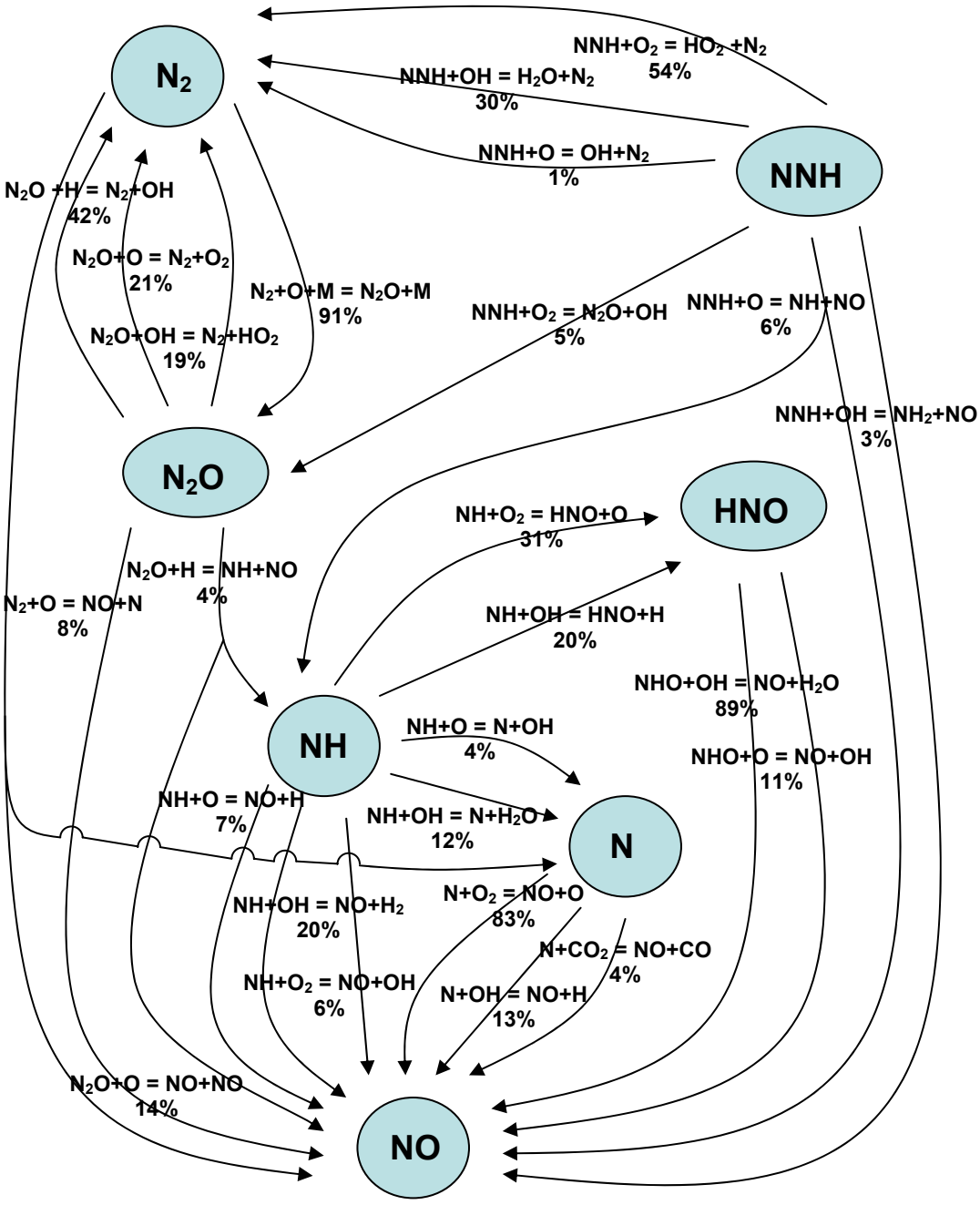

Figure 31, Nodal Diagram of Destruction to NO in PST with Modified Tomeczek and Gradoń Mechanism

The nodal diagrams show that each mechanism has similarities to and differences from the other two. For all three mechanisms, the Zeldovich pathway is present only in the second element, where the temperature is sufficiently high. Figure 29 shows that the Zeldovich pathway is most prominent in the UCSD mechanism. Both the GRI and UCSD mechanisms show more N_2 reacting to NNH and a less significant amount reacting to N_2O. In the PST element in both mechanisms, however, more N_2 reacts to N_2O and a less to NNH. The modified Tomeczek and Gradoń mechanism shows a different trend. Of the N_2 reacting in the PSB, 95% reacts to N_2O while only 5% reacts to NNH. The percentage of N_2 reacting to NNH in the PST element using the modified Tomeczek and Gradoń mechanism is trivial.

Figure 26 shows that in the PSB of GRI 3.0, 66% of the reacting N_2 destructs to NNH. Also, 12% of the destructing NNH reacts by NNH+O=NH+NO where all NH subsequently reacts to NO, affectively doubling the influence of this reaction on NO production. Thus, the percentage of destructing N_2 that reacts though this pathway greatly influences NO_x prediction in GRI 3.0. The NNH pathway in the UCSD and modified Tomeczek and Gradoń mechanisms is not as influential. In the UCSD mechanism, while the amount of destructing N_2 which reacts to NNH in the PSB is still high (57%), only 1% of the destructing NNH reacts directly to NO. Instead, 49% of destructing NNH reacts to N_2O – a pathway not present in GRI. Because only 3-4% of N_2O reacts to NO and NH, the NNH reacting to N_2O first, and not directly to NO, forms significantly less NO_x. In the Tomeczek and Gradoń mechanism, 24% of the destructing NNH reacts to NO by NNH+OH=NH+NO. But, the amount of NO produced by this pathway is limited because only 5% of the destructing N_2 reacts to NNH.

Pathway Contributions

Additional insight on the NO_x formation pathways of each mechanism is obtained by analyzing the pathways at both pressures (1 atm and 6.5 atm) for high and low CO/H_2

ratios. The NO_x contribution from each pathway is determined by comparing the total predicted NO_x with that predicted after suppressing the initiating reactions of the pathway. The initiating reactions are shown in the nodal diagrams in Figures 26-31. The reactions were suppressed by setting their corresponding rate constants to zero in the mechanism. The difference between the total NO_x predicted and the NO_x predicted with one pathway suppressed is the contribution of that pathway. The reactions suppressed for each pathway are:

Zeldovich Pathway:	$N_2 + O = NO + N$
N_2O Pathway:	$N_2 + O + M = N_2O + M$
NNH Pathway:	$N_2 + H = NNH$
	$N_2 + H + M = NNH + M$

Table 14 shows the overall NO_x contributions of each pathway for the elements combined. The three mechanisms are analyzed at 6.5 atm and for both $CO/H_2 = 0.5$ and $CO/H_2 = 3.2$.

Table 14, NO_x Contributions by Pathway for Combined Elements at 6.5 atm

	GRI 3.0		UCSD		Modified Tomeczek and Gradoń	
NO_x Pathway	**$CO/H_2 = 0.5$**	**$CO/H_2 = 3.2$**	**$CO/H_2 = 0.5$**	**$CO/H_2 = 3.2$**	**$CO/H_2 = 0.5$**	**$CO/H_2 = 3.2$**
Zeldovich (%)	20	16	57	45	30	19
N_2O (%)	36	55	39	52	60	77
NNH (%)	44	29	4	3	10	4

Consistent with the UCSD PST nodal diagram, Table 14 shows that the Zeldovich pathway contributes a higher percentage of NO_x in the UCSD mechanism than in the GRI 3.0 and modified Tomeczek and Gradoń mechanisms. The modified Tomeczek and Gradoń mechanism exhibits the most NO_x formed by the N_2O pathway, as suggested by the high percentage of destructing N_2 forming N_2O in the nodal diagrams.

The UCSD and modified Tomeczek and Gradoń mechanisms have similar contributions, 3-10%, from the NNH pathway. In GRI, however, the percentage of NO_x produced by the NNH pathway is substantially greater. As shown above, the larger GRI contribution from the NNH pathway is due to both the high percentage of destructing N_2 forming NNH and the direct reaction of NNH to NH and NO. The overall tendency of GRI 3.0 to over predict NO_x may be largely due to the contribution from its NNH pathway.

All three mechanisms show a greater contribution from the N_2O pathway at the higher CO/H_2 ratio. For the GRI mechanism, this is at the expense of the NNH pathway; for the UCSD and modified Tomeczek and Gradoń mechanisms this is at the expense of the Zeldovich pathway. Table 15 shows the NO_x contributions by pathway at 1 atm.

Table 15, NO_x Contributions by Pathway for Combined Elements at 1 atm

	GRI 3.0		UCSD		Modified Tomeczek and Gradoń	
NO_x Pathway	**$CO/H_2 = 0.33$**	**$CO/H_2 = 3$**	**$CO/H_2 = 0.33$**	**$CO/H_2 = 3$**	**$CO/H_2 = 0.33$**	**$CO/H_2 = 3$**
Zeldovich (%)	21	22	70	69	36	39
N_2O (%)	31	30	18	17	54	50
NNH (%)	48	48	12	14	10	11

At 1 atm, the fuel molar ratio has little effect on the NO_x formation pathways. For the GRI 3.0 and the modified Tomeczek and Gradoń mechanisms, the pathway contributions at 1 atm are fairly close to those at 6.5 atm for $CO/H_2 = 0.5$, as shown in Table 14. In the UCSD mechanism, however, the sizeable contribution from the N_2O pathway at 6.5 atm is reduced by a factor of 2 to 3 at 1 atm and the Zeldovich mechanism is more prominent. At 1 atm, the UCSD and modified Tomeczek and Gradoń mechanisms agree very well on the low contribution of the NNH pathway, as with the 6.5 atm results. While the dominant pathway for the UCSD mechanism is the Zeldovich, however, that for the modified Tomeczek and Gradoń mechanism is N_2O.

Section 6: Discussion and Summary

Discussion

This work shows that NO_x measurements taken by Malte[6] and Horning[8] in jet-stirred reactor experiments with CO/H_2 fuels show significant trends. The trends in the data show that NO_x emission increases with increasing CO/H_2 ratio, increasing preheat temperature, and decreasing pressure. The NO_x and CO measurements at 1 atm and 6.5 atm and CO/H_2 fuel ratios between 0.33 and 3.2 provide an adequate database for judging the usefulness of a chemical reactor model for predicting NO_x and CO near residence times of 4 ms, temperatures near 1800 K, and equivalence ratios near 0.6.

An initial element configuration of PSB+PST+PFT was used. The turbulent flame volume was calculated using the flame speeds of the fuel-air mixtures for the conditions of each experiment. Then, the flame volume was used as an approximation of the size of the first reactor element. At 6.5 atm, the PSB size was the same as the flame volume calculation for low CO/H_2 fuel ratios. As the CO/H_2 ratio was increased, however, the PSB size grew and exceeded the flame volume calculation. Thus, it was not possible to use the calculated flame volume in these chemical reactor setups. The element configuration was completed by matching the model predictions of CO with experimental CO measurements and determining that a 7% PFT is necessary to provide sufficient relaxation of CO in the recirculation zone. At 6.5 atm, GRI 3.0 only predicts NO_x concentrations close to experimental values at high CO/H_2 fuel ratios. The UCSD mechanism only predicts closely at low CO/H_2 fuel ratios. The modified Tomeczek and Gradoń mechanism successfully fits the overall trend in the data, predicting NO_x within 1.13 ppm at all fuel molar ratios. The CO predictions of the mechanism also match experimental data well. This study shows that, of the mechanisms tested, the modified Tomeczek and Gradoń mechanism using a PSB+PST+PFT(7%) reactor configuration is most successful in predicting measurements of NO_x and CO at 6.5 atm.

At 1 atm, the GRI 3.0 mechanism significantly over predicts NO_x. The UCSD mechanism more closely predicts measurements, under predicting NO_x by about 2 ppm for nominal NO_x levels between 6.6 and 10.7. The modified Tomeczek and Gradoń mechanism, again, matches the experimental results best, over predicting by less than 2 ppm. The close prediction of the modified Tomeczek and Gradoń mechanism to measurements is maintained at higher preheat temperatures. The mechanism significantly over predicts CO concentrations, however, using a 7% PFT. In addition, the flame volume calculations show that the PSB element is too small to match the 5% flame volume of the reactor. For these reasons, alternative element configurations were tested at 1 atm. A larger PFT element of 17.5% lowered CO predictions to measured values. The 5% flame region was modeled both by a 5% PSR, and by a combination of a PSB and PSR, together representing 5% of the reactor volume. These two representations give very similar NO_x predictions. Overall, the modified Tomeczek and Gradoń mechanism using a PSR(5%)+PST+PFT(17.5%) or a PSB+PSR(5%)+PST+PFT(17.5%) reactor configuration predicts NO_x measurements closely at 1 atm for preheat temperatures of 423-523 K.

In order to determine the differences in the NO_x formation pathways of each mechanism, nodal diagrams were constructed and individual pathways were suppressed in the model. Both of these methods show similarities and differences among all three mechanisms. The outstanding difference, however, among the mechanisms is that the percentage of NO_x formed by the NNH pathway is small in the UCSD and Tomeczek and Gradoń mechanisms, but large in the GRI 3.0 mechanism. The large contribution of the NNH pathway in GRI 3.0 is due to both the large percentage of destructing N_2 that forms NNH and the strong influence of the reacting NNH on NO_x formation. The over prediction of NO_x by GRI is primarily due to the large role of its NNH pathway.

Summary: Impact of Research

This thesis provides insight on the effectiveness of several element configurations and three mechanisms for the modeling of NO_x and CO in lean-premixed, high-intensity CO/H_2 combustion at 1 atm and 6.5 atm. Modeling NO_x production in CO/H_2 fuels, like those produced as synthesis gas from coal, is necessary in order to develop cleaner energy production using integrated gasification combined cycle power plants. This work and additional research in this area are important steps in making IGCC plants a cost-effective, energy-independent, and clean method for meeting our nation's increasing energy needs.

BIBLIOGRAPHY

1. National Energy Policy Development Group. "Reliable, Affordable, and Environmentally Sound Energy for America's Future." U.S. Department of Energy. 12 July 2004 <http://www.energy.gov/engine/doe/files/dynamic/1952003121758_national_energy_policy.pdf>.
2. Energy Information Administration. "Exploration and Reserves." EIA Natural Gas. 12 July 2004 <http://tonto.eia.doe.gov/dnav/ng/ng_enr_dry_dcu_NUS_a.htm>.
3. Brun, K. "Environmental Benefits of IGCC Coal Power Plant: A Technology Comparison." ASME Turbo Expo (2002).
4. Lefebvre, A.H. Gas Turbine Combustion. Philadelphia: Taylor & Francis, 1999.
5. Smith, Gregory P., Golden, David M., Frenklach, Michael, Moriarty, Nigel W., Eiteneer, Boris, Goldenberg, Mikhail, Bowman, C. Thomas, Hanson, Ronald K., Song, Soonho, Gardiner Jr., William C., Lissianski, Vitali V., and Qin, Zhiwei. "Current and Future Releases of GRI-Mech." GRI-Mech^{TM}. Serauskas, Bob. Version GRI 3.0. Gas Research Institute. 30 May 2004 <http://www.me.berkeley.edu/gri_mech/index.html>.
6. Malte, P.C. "Re: JSR Experiments and Data Spreadsheets." Personal Communication to Gwenn Heyer. 30 May 2004.
7. Jarrett, A.C. "NO_x Formation in Lean-Premixed Combustion." Master's Thesis, University of Washington (1995).
8. Horning, David C. "Pollutant Formation by Lean-Premixed Combustion in a High Pressure Jet-Stirred Reactor." Master's Thesis, University of Washington (1996).
9. Rutar, T., Malte, Philip C., and Kramlich, John C. "Investigation of NO_x and CO Formation in Lean-Premixed, Methane-Air, High-Intensity, Confined Flames at Elevated Pressures." 28th Symposium (International) on Combustion (2000).
10. Rutar, T. and Malte, Philip C., "NO_x Formation in High-Pressure Jet-Stirred Reactors with Significance to Lean-Premixed Combustion Turbines." Proceedings of ASME (2001).
11. Schmid, H-P., Habisruether, P., and Leuckel, W., "A Model for Calculating Heat Release in Premixed Turbulent Flames." Combustion and Flame 113 (1998): 79-91.
12. McLean, Ian C., Smith, David B., and Taylor, Simon C. "The Use of Carbon Monoxide/Hydrogen Burning Velocities to Examine the Rate of the CO + OH Reaction." 25th Symposium (International) on Combustion (1994): 749-757.
13. Glasman, I. Combustion. San Diego: Academic Press, 1996.
14. Turns, Steven R. An Introduction to Combustion. Boston: McGraw-Hill, 2000.
15. Williams, Forman A. "University of California, San Diego, Center for Energy Research." Chemical Kinetic Mechanisms for Combustion Applications. 13 July 2004 <http://maemail.ucsd.edu/combustion/cermech/>.

16. Tomeczek, J. and Gradoń B., "The Role of N_2O and NNH in the Formation of NO via HCN in Hydrocarbon Flames." Combustion and Flame 133 (2003): 311-322.
17. Glarborg, et al., "Kinetics of Homogeneous Nitrous Oxide Decomposition." Combustion and Flame 99 (1994): 523-532.
18. Michael, J. V. and Lim K. P., "Rate Constants for the N_2O Reaction System: Thermal Decomposition of N_2O; $N+NO \rightarrow N_2+O$ and Implications for $O+N_2 \rightarrow NO+N$." Journal of Chemical Physics 97 (1992) 3228-3234.
19. Tomeczek, J. and Gradoń B., "The Role of Nitrous Oxide in the Mechanism of Thermal Nitric Oxide Formation within Flame Temperature Range." Combustion Science and Technology 125 (1997): 159-180.
20. Lee, John C.Y., Malte, Philip C., and Benjamin, Michael A., "Low NO_x Combustion for Liquid Fuels: Atmospheric Pressure Experiments Using a Staged Prevaporizer-Premixer." Transactions of the ASME, Journal of Engineering for Gas Turbines and Power 125 (2003): 861-871.
21. Steele, R. C. "NO_x and N_2O Formation in Lean-Premixed Jet-Stirred Reactors Operated from 1 to 7 atm." Ph.D. Dissertation, University of Washington (1995).

APPENDIX A

Compilation of Hydrocarbon Data

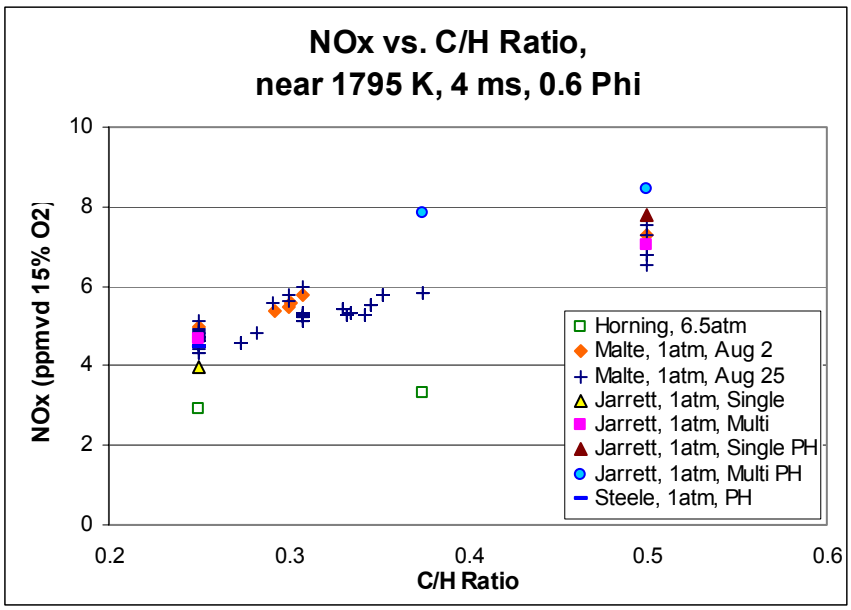

This figure shows the compilation of hydrocarbon combustion data of Horning,[8] Malte,[6] Jarrett,[7] and Steele.[21] Horning's data includes NO_x measurements for methane and propane taken for the temperature range of 1680-1890 K and residence times of 4.12-4.36 ms. His NO_x data for methane and propane are separately interpolated to 1795 K. Malte measured NO_x for the combustion of many hydrocarbon blends at temperatures between 1790-1795 K. All of his data appears in the figure. Equivalence ratios for Malte's experiments are 0.585-0.695; residence times are 3.61-4.00 ms. Jarrett's data includes measurements for methane, propane, and ethylene. His measurements were taken over the temperature range of 1518-1798 K with residence times of 3.44-4.12 ms. His single nozzle data (room temperature and 600 K preheated) and multi nozzle data (room temperature and 600 K preheated) are shown separately. Jarrett's equivalence ratios, 0.391-0.680, varied significantly. Steele's methane measurements were taken between 1649-1800 K with preheat temperature of 600 K. Residence times for Steele's

experiments are 3.22-3.54 ms; equivalence ratios are 0.517-0.617. Steele's NO_x data for varying temperature was interpolated to 1795 K.

The figure shows that for a given C/H ratio, Horning's high pressure NO_x measurements are lower than those at atmospheric pressure. Steele's NO_x measurements for methane show close agreement to Malte's NO_x measurements at C/H = 0.25. Because NO_x production is affected by equivalence ratio, the large range of equivalence ratios used in Jarrett's experiments leads to scatter in his NO_x measurements. Therefore, the interpolation of Jarrett's data to 1795 K is discounted and his measurements cannot be compared effectively to the measurements of Horning, Malte, and Steele at 1795 K.

The hydrocarbon measurements show trends in agreement with CO/H_2 measurements. First, NO_x emission increases with increasing C/H ratio. Second, NO_x emission decreases with increasing pressure. This implies that similar NO chemistry may be controlling the formation and emission of NO_x in hydrocarbon and CO/H_2 combustion.

APPENDIX B

Modified Tomeczek and Gradoń Mechanism

Rate Constant, $k = k_0 T^n \exp(-E/RT)$

No.	Reaction	k_0 $\log_{10}[cm^3/(K^{-n}mol \cdot s)]$	n	E kcal/kmol
1	N+NO = N2+O	13.431[a]	0.00[a]	0.355[a]
2	N+O2 = NO + O	9.806	1.00	6.260
3	N2O+M = N2+O+M	14.505[b]	0.00[b]	55.480[b]
	N2O+M = N2+O+M, pressure	14.804[c]	0.00[c]	56.640[c]
4	N2O+O = NO+NO	13.462[a]	0.00[a]	23.150[a]
5	N2O+O = N2+O2	12.146[a]	0.00[a]	10.810[a]
6	NH+NO = N2O+H	16.398	-1.03	0.834
7	N2O+H = N2+OH	14.342	0.00	16.754
8	N2O+OH = N2+HO2	11.215	0.00	9.935
9	NNH+M = N2+H+M	14.114	-0.11	4.981
10	NNH+O = NO+NH	13.519	-0.23	-1.011
11	NNH+O2 = N2O+OH	11.462	-0.34	0.148
12	NNH+O = N2O+H	14.146	-0.40	0.476
13	NNH+H = N2+H2	11.000	0.00	0.000
14	NNH+OH = N2+H2O	22.380	-2.88	2.445
15	NNH+O = N2+OH	16.230	-1.23	0.497
16	NNH+O2 = N2+HO2	12.079	-0.34	0.148
17	NNH+NO = N2+HNO	13.699	0.00	0.000
18	NNH+NH = N2+NH2	13.699	0.00	0.000
19	NNH+NH2 = N2+NH3	13.699	0.00	0.000
20	NO2+M = NO+O+M	16.041	0.00	65.574
21	NO2+H = NO+OH	13.926	0.00	0.000
22	NO2+O = NO+O2	12.592	0.00	0.239
23	NO+HO2 = NO2+OH	12.324	0.00	-0.480
24	NH+O2 = NO+OH	10.881	0.00	1.532
25	NH+O = NO+H	13.740	0.00	0.000
26	NH+OH = N+H2O	11.699	0.50	2.000
27	NH+N = N2+H	13.477	0.00	0.000
28	NH+O = N+OH	13.571	0.00	0.000
29	NH+NO = N2+OH	13.334	-0.23	0.000
30	N+H2 = NH+H	14.204	0.00	25.158
31	NH+NH = N2+H+H	13.708	0.00	0.000
32	NH+OH = NO+H2	13.301	0.00	0.000
33	NH+O2 = HNO+O	13.590	0.00	17.897
34	NH+OH = HNO+H	13.301	0.00	0.000
35	HNO+M = NO+H+M	16.176	0.00	48.714
36	HNO=OH = NO+H2O	13.681	0.00	0.989
37	HNO+O = NO+OH	13.558	0.00	0.000
38	HNO+H = H2+NO	13.258	0.00	0.994
39	HNO+HNO = N2O+OH	12.597	0.00	5.002

40	HNO+NO = N2O+OH	12.301	0.00	26.018
41	N+OH = NO+H	13.580	0.00	0.000
42	NH2+O = OH+NH	12.845	0.00	0.000
43	NH2+O = HNO+H	14.822	-0.50	0.000
44	NH2+OH = NH+H2O	6.602	2.00	1.001
45	NH2+NO = NNH+OH	15.806	-1.25	0.000
46	NH2+NO = N2+H2O	18.792	-1.25	0.000
47	NH2+N = N2+H+N	13.857	0.00	0.000
48	NH2+O2 = HNO+OH	12.653	0.00	25.017
49	NH2+H = NH+H2	13.840	0.00	3.652
50	NH2+HNO = NH3+NO	13.301	0.00	1.001
51	NH2+M = NH2+H+M	16.146	0.00	90.664
52	NH3+M = NH+H2+M	16.699	0.00	81.262
53	NH3+H = NH2+H2	5.806	2.39	10.179
54	NH3+OH = NH2+H2O	6.310	2.04	0.566
55	NH3+O = NH2+OH	13.322	0.00	9.006
82	NCO+H = NH+CO	13.699	0.00	0.000
83	NCO+O = NO+CO	13.301	0.00	0.000
84	NCO+N = N2+CO	13.301	0.00	0.000
85	NCO+M = N+CO+M	16.491	-0.50	48.040
86	NCO+NO = N2O+CO	13.000	0.00	-0.390
87	NCO+OH = NO+CO+H	13.000	0.00	0.000
88	N+CO2 = NO+CO	11.279	0.00	3.403
93	CN+O = CO+N	13.255	0.00	0.000
94	CN+O2 = NCO+O	12.748	0.00	0.000
95	CN+OH = NCO+NO	13.778	0.00	0.000
96	CN+NO2 = NCO+NO	13.477	0.00	0.000
97	CN+N2O = NCO+N2	13.000	0.00	0.000

[a] GRI constants used, previous constants for fuels with no hydrogen

[b] Used constants suggested by Glarborg et al. for appropriate temperature

[c] GRI constants used along with Glarborg et al. constants to incorporate pressure dependence